Report No.
UCB/SEMM-2013/09

Structural Engineering
Mechanics and Materials

An Efficient Time-Domain Perfectly Matched Layers Formulation for Elastodynamics on Spherical Domains

By

Koki Sagiyama, Sanjay Govindjee, and Per-Olof Persson

November 2013

Department of Civil and Environmental Engineering
University of California, Berkeley

Abstract

Many practical applications require the analysis of elastic wave propagation in a homogeneous isotropic media in an unbounded domain. One widely used approach for truncating the infinite domain is the so-called method of Perfectly Matched Layers (PMLs). Most existing PML formulations are developed for finite difference methods based on the first-order velocity-stress form of the elastic equations and they are not straight-forward to implement using standard finite element methods on unstructured meshes. Some of the problems with these formulations include the application of boundary conditions in half-space problems and in the treatment of edges and/or corners for time-domain problems. Several PML formulations which do work with finite element methods have been proposed, although most of them still have some of these problems and/or they require a large number of auxiliary nodal history/memory variables. In this work we develop a new PML formulation for time-domain elastodynamics on a spherical domain, which reduces to a two-dimensional formulation under the assumption of axisymmetry. Our formulation is well-suited for implementation using finite element methods, where it requires lower memory than existing formulations and it allows for natural application of boundary conditions. We solve example problems on two- and three-dimensional domains using a high-order discontinuous Galerkin discretization on unstructured meshes and explicit time-stepping. We also study an approach for stabilization of the discrete equations and we show several practical applications for quality factor predictions of micromechanical resonators along with verifying the accuracy and versatility of our formulation.

Keywords: PML; perfectly matched layer; elastodynamics; Discontinuous Galerkin; stabilization.

An Efficient Time-Domain Perfectly Matched Layers Formulation for Elastodynamics on Spherical Domains

Koki Sagiyama, Sanjay Govindjee, and Per-Olof Persson
Department of Civil Engineering, University of California, Berkeley
Department of Mathematics, University of California, Berkeley

November 5, 2013

1 Introduction

The analysis of wave propagation in an unbounded domain is of interest in many fields, such as geotechnical engineering and electromechanics. Due to the unboundedness, these problems do not allow for direct application of standard numerical schemes such as finite element methods which require a finite computational domain. Therefore, they require new methodologies or a mapping of the problem to a finite domain. Within the class of mapped methods, the so-called perfectly matched layer (PML) methods have become popular due to their simplicity of implementation, accuracy, and versatility. In the PML method, the unbounded domain is truncated and an artificial PML region is attached, resulting in a finite physical domain. In a continuous setting, provided that the PML region is of infinite depth, outgoing waves travel into the PML with no spurious reflections back into the physical domain and they rapidly attenuate within the PML domain. While reflections do arise in numerical computations due to discretization effects as well as finite depth effects, relatively shallow PMLs usually suffice to achieve a satisfactory level of accuracy, as has been widely seen in many fields over the last two decades.

This paper focuses on an efficient PML formulation for time-domain elastodynamics on spherical domains in 3-D, or axisymmetric domains in 2-D. Our main motivation is the development of an efficient high-fidelity radiation boundary condition suitable for anchor-loss simulations of MEMS-resonator systems [1, 2, 3], where a set of resonating bodies is attached to an unbounded substrate via a cylindrical posts with small radii. These types of structures emits elastic waves almost spherically into the substrate from the bottom-end of the support posts/anchors. Therefore, it is natural to truncate the substrate spherically around the posts, resulting in a semi-half sphere, since PMLs exhibit best absorption for waves of normal incidence. On the other hand, for applications such as seismic-wave propagation caused by a fault-rupture which often takes place along a plane, the radius of truncation must be large enough to include all the rupture-surface. Our spherical PML might then not give as good efficiency, since it will also include a large portion of the domain that is less relevant.

The PML method was developed by Berenger [4] for time-domain electromagnetics on an unbounded domain. The electromagnetic fields are decomposed into non-physical components according to their spatial derivatives and artificial damping terms are added to a set of so-called split equations outside the domain of interest such that outgoing waves are absorbed. The addition of artificial damping was later identified by Chew and Weedon as a complex coordinate transformation in the frequency-domain [5], where one could readily inverse-transform the resulting system into the time-domain without producing computationally expensive convolution integrals. The idea of field-splitting followed by a complex transformation of coordinate systems was soon adopted in time-domain elastodynamics written in the first-order velocity-stress form[1] [6, 7, 8, 9]; It was observed, however, that the classical complex transformation functions in [5] tended to

[1] It should be noted that the PML formulations thus obtained involve non-physical splitting of the equations and also involve the use of stresses as primary unknowns, both of which can make enforcement of boundary conditions quite difficult.

produce large spurious reflections into physical domains if waves were strongly evanescent and/or hit the PML with grazing incident angles. To resolve these issues, the Complex-Frequency-Shifted PML (CFS-PML) method was proposed in [10]. This is a class of PMLs that uses more general complex transformation functions than those in [5]. We will denote PML formulations that uses the original transformation functions as 'Classical-PMLs' as opposed to CFS-PMLs.

The traditional PML formulation that employs splitting of the fields, however, is not suitable for CFS-PML since it requires convolutions for the inverse-transformation into the time-domain. Furthermore, splitting of the fields introduces two distinct sets of equations on the physical and the PML domains, requiring a special treatment of the interface between the two. To circumvent these issues and employ CFS-PML, unsplit convolution-PML (C-PML) was developed by Roden and Gedney [11] and it has been used as an alternative to the traditional field-splitting PML. C-PML is based on a direct inverse Fourier transform of the complex-transformed equations into the time-domain which produces convolutions. These convolutions are then approximated by the recursive convolution method [12], where they are evaluated by introducing additional unknowns and solving second-order recursions at each time-step. C-PML was first used for time-domain electromagnetics in [11] and since then it has been adopted for time-domain elastodynamics in [13, 14, 15]; it has been demonstrated that CFS-PML used with C-PML exhibits considerable improvement in accuracy against evanescent and grazing waves over Classical PML. Auxiliary-differential-equation PML (ADE-PML) uses differential equations instead of recursions and surpasses C-PML in the point that it can be arbitrarily high-order in time. It was first applied to electromagnetics with Classical PML in [16] and with CFS-PML in [17]. It has also been applied in elastodynamics with CFS-PML in [18, 19, 20].

It is worth noting that the ADE-PML formulations in [18, 19, 20] can be regarded as perturbations of the original velocity-stress formulation of elastodynamics; i.e., the physical domain is governed by the same set of equations as the PML domain with all auxiliary variables set to zero, which leaves the standard velocity-stress formulation in the physical domain and makes the implementation easier. It should also be noted that all these formulations, when applied to three-dimensional elastodynamics, have 9 degrees of freedom (DOFs) in the physical domain, 15 on the faces, 21 on the edges, and 27 at the corners. In addition, extra effort is required to apply traction-free boundary conditions on free-surface PML boundaries as mentioned in [20].

All of these PML formulations for elastodynamics are based on the first-order velocity-stress formulation, which is well-suited for discretization using finite difference methods. However, for computational domains with complex geometries, numerical methods based on fully unstructured meshes such as finite element methods are often preferred. Several efforts have been made to develop such PML formulations in the frequency-domain [21, 22] and in the time-domain [23, 24, 25, 26, 27, 28, 29, 30]. Among the time-domain formulations, those developed in [26, 27, 29, 30] possess a strong advantage over others including the ones based on the velocity-stress formulation. By not decomposing the divergence operator, they yield explicit boundary traction integrals in their weak formulations as a result of the divergence theorem. Thus Neumann boundary conditions can be naturally applied. This makes the implementation considerably easier when an unbounded half-space is to be truncated by a PML and a traction-free boundary condition has to be applied on a surface of the PML. However, a common drawback of these formulations is that they require a large number of auxiliary nodal history/memory variables. For example, the formulation in [27] applied on a three-dimensional rectangular domain requires memory for displacement, velocity, strain, strain-history, stress-history, history of stress-history, and, at corners, displacement-history, for a total of 33 DOFs at a corner region in the PML and 30 DOFs elsewhere in the PML domain. Further, these formulations have two distinct structures in the physical and the PML domains, which necessitates a special treatment of the interface between the two.

Here, we present a PML formulation that is developed for three-dimensional domains which are truncated with a spherical boundary in which a complex-coordinate transformation is performed *solely* in the radial direction. Although transformations are usually done in directions parallel to the Cartesian coordinate axes, for many applications it is advantageous to do it along radial axes since this does not involve edges or corners which require specialized treatments in the time-domain. Our formulation is based on the frequency-domain formulation presented in [22] and it is compatible with standard finite element methods and discontinuous Galerkin methods on unstructured meshes. The formulation uses only 6 DOFs in the physical domain and

12 DOFs in the PML domain for three-dimensional elasticity written as a first-order system in time. The physical domain is governed by the same equation as in the PML domain with the auxiliary variables turned off, as is the case in [18, 19, 20]. Physical traction-free boundary conditions are naturally applied on PML surfaces as in [26, 27, 29, 30]. Moreover, using a discontinuous Galerkin method with second-derivatives based on the Compact Discontinuous Galerkin (CDG) scheme, the mass matrices can be explicitly inverted with small computational effort which enables the use of explicit time-integrators such as explicit Runge-Kutta methods without the loss of accuracy that typically accompanies explicit time stepping methods that employ traditional mass lumping schemes. The complex transformation functions used in our formulation lie between Classical-PML and CFS-PML. Although it is less general than CFS-PML, our examples show its high ability to absorb quite complex waves. In our numerical examples, we observe long time exponential error growth on coarse meshes for the straight-forward Galerkin discretization using the CDG scheme. To rectify this, we propose an artificial viscosity based approach to stabilize the formulation and we show that this stabilization is only required on coarse meshes.

We derive our new formulations in Sec. 2, explain the discontinuous Galerkin discretization procedure in Sec. 3, and demonstrate its accuracy and versatility through examples in Sec. 4.

2 PML for elastodynamics

2.1 Basic concept

We briefly introduce the concept of PMLs through a one-dimensional problem in the frequency-domain using the $e^{\mathrm{i}\omega t}$ convention ($\mathrm{i}=\sqrt{-1}$). Consider the vibration of a semi-infinite ($x \geq 0$) string on an elastic base [31] with a source located at $x = 0$ and suppose we are interested in the solution for $x \in [0, x_0]$. An approximate solution to this outgoing-wave problem is obtained by solving a PML system truncated at $x = x_{pml} > x_0$:

$$\text{Find } u(x) \text{ on } x \in [0, x_{pml}] \text{ such that:}$$

$$(\mathrm{i}\omega)^2 \rho u - T\frac{d^2u}{d\tilde{x}^2} + ku = 0, \tag{1a}$$

$$u(0) = 1, \tag{1b}$$

$$u(x_{pml}) = 0, \tag{1c}$$

where the complex-valued coordinate

$$\tilde{x}(x) = x + \int_0^x f^e(s)\, ds + \frac{\omega_0}{\mathrm{i}\omega}\int_0^x f^p(s)\, ds, \quad x \in [0, x_{pml}], \tag{2}$$

and $f^p(x)$ and $f^e(x)$ are real functions of x defined such that

$$\begin{cases} f^p, f^e = 0 & \text{if } 0 \leq x \leq x_0, \\ f^p, f^e > 0 & \text{if } x > x_0, \end{cases} \tag{3}$$

for some constants $x_0 > 0$ and $\omega_0 > 0$. The constant ω_0 is introduced merely for non-dimensionalization. The complex transformation function (2) was also used as an alternative to CFS-PML in [26, 27, 29, 30]. There are two possible types of solutions to system (1) – a propagating wave solution and an evanescent wave solution depending on the sign of $k - \rho\omega^2$:

$$u(x) = \begin{cases} c^+ \exp\left[-\mathrm{i}\gamma x - \mathrm{i}\gamma \int_0^x f^e(s)ds - \gamma\frac{\omega_0}{\omega}\int_0^x f^p(s)ds\right] \\ \qquad + c^- \exp\left[+\mathrm{i}\gamma x + \mathrm{i}\gamma \int_0^x f^e(s)ds + \gamma\frac{\omega_0}{\omega}\int_0^x f^p(s)ds\right] & \text{if } k - \rho\omega^2 < 0, \\ c^+ \exp\left[-\bar{\gamma} x - \bar{\gamma} \int_0^x f^e(s)ds - \bar{\gamma}\frac{\omega_0}{\mathrm{i}\omega}\int_0^x f^p(s)ds\right] \\ \qquad + c^- \exp\left[+\bar{\gamma} x + \bar{\gamma} \int_0^x f^e(s)ds + \bar{\gamma}\frac{\omega_0}{\mathrm{i}\omega}\int_0^x f^p(s)ds\right] & \text{if } k - \rho\omega^2 > 0, \end{cases}$$

where we define γ and $\bar{\gamma}$ as:

$$\frac{k-\rho\omega^2}{T} := -\gamma^2 := \bar{\gamma}^2.$$

Note that because of definition (3), $u(x)$ on $0 \leq x < x_0$ coincides with the solution to the original half-space problem we are trying to model provided that $c^+ = 1$ and $c^- = 0$. In reality, the Dirichlet boundary condition at $x = x_{pml}$ produces a small amount of spurious reflection which pollute the solution on $0 \leq x < x_0$. The amount of reflection due to the termination of the PML is quantified by a reflection coefficient $r_{\text{termination}}$ defined as the ratio $|c^-/c^+|$:

$$r_{\text{termination}} = \begin{cases} \exp\left[-2\gamma\frac{\omega_0}{\omega}\int_0^{x_{pml}} f^p(s)ds\right] & \text{if } k-\rho\omega^2 < 0, \\ \exp\left[-2\bar{\gamma}x_{pml}\right]\cdot\exp\left[-2\bar{\gamma}\int_0^{x_{pml}} f^e(s)ds\right] & \text{if } k-\rho\omega^2 > 0. \end{cases} \tag{4}$$

From this it is clear that $f^p(x)$ and $f^e(x)$ control the absorption of propagating and evanescent waves, respectively, and $r_{\text{termination}} \to 0$, and thus $c^+ \to 1$ and $c^- \to 0$, as one increases $f^p(x)$, $f^e(x)$, and/or x_{pml}. In a continuous setting, the reflection due to termination can be made arbitrarily small with no additional computational effort by increasing $f^p(x)$ and/or $f^e(x)$, but in approximate numerical computations another type of reflection arises due to the spatial discretization, denoted by $r_{\text{discretization}}$. With rapid changes of $f^p(x)$ and $f^e(x)$ in space, $r_{\text{discretization}}$ increases. Therefore, one has to find a compromise between these competing effects in order to minimize the *total* reflection in an actual numerical solution.

For later application we rewrite Eqn. (1a) in terms of x to obtain a total system:

$$\begin{aligned} &\text{Find } u(x) \text{ on } x \in [0, x_{pml}] \text{ such that:} \\ &(\mathrm{i}\omega)^2 \rho u - T\frac{1}{s}\frac{d}{dx}\left(\frac{1}{s}\frac{du}{dx}\right) + ku = 0, && \text{(5a)} \\ &u(0) = 1, && \text{(5b)} \\ &u(x_{pml}) = 0, && \text{(5c)} \end{aligned}$$

where

$$s(x) = 1 + f^e(x) + \frac{\omega_0}{\mathrm{i}\omega} f^p(x). \tag{6}$$

This PML system is the actual form that one discretizes for numerical solutions.

2.2 General formulation

Next, we present a general formulation of PMLs for time-harmonic elasticity following [22]. This formulation will be the starting point for our new developments. We consider the problem of elasticity on an unbounded domain $(x_1, x_2, x_3) \in \Omega_\infty$ in which we are interested in the solution on $\Omega_0 \subset \Omega_\infty$, where $\text{vol}(\Omega_0) < \infty$. Ω_∞ is truncated and a PML region is attached to the artificial truncation boundary, producing a finite computational domain $\Omega \supset \Omega_0$. The problem statement is given as:

$$\begin{aligned} &\text{Find } \boldsymbol{u}(x_1, x_2, x_3) \text{ for } (x_1, x_2, x_3) \in \Omega \text{ such that:} \\ &(\mathrm{i}\omega)^2 \rho \boldsymbol{u} - \tilde{\boldsymbol{\nabla}} \cdot \tilde{\boldsymbol{\sigma}}^T = \boldsymbol{f}, && \text{(7a)} \\ &\tilde{\boldsymbol{\sigma}} = \mathsf{C} : \tilde{\boldsymbol{\epsilon}}, && \text{(7b)} \\ &\tilde{\boldsymbol{\epsilon}} = \frac{1}{2}[\tilde{\boldsymbol{\nabla}}\boldsymbol{u} + \tilde{\boldsymbol{\nabla}}\boldsymbol{u}^T], && \text{(7c)} \\ &\boldsymbol{u} = \bar{\boldsymbol{u}} \quad \text{on } \partial\Omega_u, \\ &\tilde{\boldsymbol{\sigma}}^T \tilde{\boldsymbol{n}} = \tilde{\boldsymbol{t}} \quad \text{on } \partial\Omega_t, \end{aligned}$$

where $\partial\Omega_u \cup \partial\Omega_t = \partial\Omega$ and $\partial\Omega_u \cap \partial\Omega_t = \phi$, $\tilde{\boldsymbol{n}}$ is the outward normal to $\partial\Omega$, C is the stiffness tensor, and $\tilde{\boldsymbol{\nabla}}$, $\tilde{\boldsymbol{\epsilon}}$ and $\tilde{\boldsymbol{\sigma}}$ are the gradient operator, the strain tensor, and the stress tensor in the $\tilde{x}$-coordinate system. Analogous to Eqn. (2), a complex-valued transformation of the coordinate system is defined with a set of functions χ_i as:

$$\tilde{x}_i = \chi_i(x_1, x_2, x_3), \quad i = 1, 2, 3, \tag{8}$$

where $\chi_i = x_i$ for $(x_1, x_2, x_3) \in \Omega_0$. We denote $\tilde{\Omega} = \{(\tilde{x}_1, \tilde{x}_2, \tilde{x}_3) : (x_1, x_2, x_3) \in \Omega\}$. The Jacobian of the transformation (8) is denoted by $\boldsymbol{\Lambda}$ so that

$$\tilde{\boldsymbol{V}} = \boldsymbol{\Lambda}\boldsymbol{V}, \tag{9}$$

where $\boldsymbol{V}$ is a tangent vector in $\mathbb{R}^3$ and $\tilde{\boldsymbol{V}}$ is its image under the coordinate transformation (8). $\boldsymbol{\Lambda}$ is assumed to be everywhere continuous and everywhere invertible for $(x_1, x_2, x_3) \in \Omega$.

As was done in Sec. 2.1, Eqn. (7a) is rewritten in terms of x_i. To this end, it is simpler to rewrite Eqn. (7a) in a weak form by applying a test function $\boldsymbol{w}$ and integrating the equation over $\tilde{\Omega}$. Applying the divergence theorem, this gives:

$$\begin{aligned}(\mathrm{i}\omega)^2 \int_{\tilde{\Omega}} \rho \boldsymbol{w} \cdot \boldsymbol{u} d\tilde{\Omega} + \int_{\tilde{\Omega}} \tilde{\boldsymbol{\nabla}} \boldsymbol{w} : \tilde{\boldsymbol{\sigma}}^T d\tilde{\Omega} \\ - \int_{\tilde{\Gamma}} \boldsymbol{w} \cdot \tilde{\boldsymbol{\sigma}}^T \tilde{\boldsymbol{n}} d\tilde{\Gamma} = \int_{\tilde{\Omega}} \boldsymbol{w} \cdot \boldsymbol{f} d\tilde{\Omega}, \quad \forall \boldsymbol{w},\end{aligned} \tag{10}$$

where $\tilde{\Gamma} = \partial\tilde{\Omega}$. Given the transformation rules for volumes, $d\tilde{\Omega} = \det \boldsymbol{\Lambda} d\Omega$, and for gradient operators,

$$\tilde{\boldsymbol{\nabla}} \boldsymbol{u} = \boldsymbol{\nabla} \boldsymbol{u} \cdot \boldsymbol{\Lambda}^{-1}, \tag{11}$$

Eqn. (10) can be transformed into the x-coordinate system as:

$$\begin{aligned}(\mathrm{i}\omega)^2 \int_{\Omega} \rho \boldsymbol{w} \cdot \boldsymbol{u} \det \boldsymbol{\Lambda} d\Omega + \int_{\Omega} \left(\boldsymbol{\nabla} \boldsymbol{w} \cdot \boldsymbol{\Lambda}^{-1}\right) : \tilde{\boldsymbol{\sigma}}^T \det \boldsymbol{\Lambda} d\Omega \\ - \int_{\Gamma} (\det \boldsymbol{\Lambda}) \boldsymbol{w} \cdot \tilde{\boldsymbol{\sigma}}^T \boldsymbol{\Lambda}^{-T} \boldsymbol{n} d\Gamma = \int_{\Omega} \boldsymbol{w} \cdot \boldsymbol{f} \det \boldsymbol{\Lambda} d\Omega, \quad \forall \boldsymbol{w},\end{aligned}$$

which by the localization theorem, yields

$$(\mathrm{i}\omega)^2 \rho \boldsymbol{u} \det \boldsymbol{\Lambda} - \boldsymbol{\nabla} \cdot [(\det \boldsymbol{\Lambda}) \boldsymbol{\Lambda}^{-1} \cdot \tilde{\boldsymbol{\sigma}}]^T = \boldsymbol{f} \det \boldsymbol{\Lambda}, \quad \boldsymbol{x} \in \Omega. \tag{12}$$

The coordinate transformation of Eqns. (7b) and (7c) are straightforward using Eqn. (11).

2.3 Spherical PML

We now specialize Eqn. (12) for a spherical coordinate system. Note that while we develop our formulation in a spherical coordinate system, the actual implementation is done in a standard Cartesian coordinate system. In other words, spherical coordinates are only used to facilitate the theoretical developments.

Since we only apply the complex transformation in the radial direction, we let:

$$\begin{aligned}(x_1, x_2, x_3) &= (r, \theta, \phi), \\ (\tilde{x}_1, \tilde{x}_2, \tilde{x}_3) &= (\tilde{r}, \theta, \phi).\end{aligned}$$

The complex transformation is defined as:

$$\tilde{r} = r + \int_0^r f^e(r) dr + \frac{\omega_0}{\mathrm{i}\omega} \int_0^r f^p(r) dr, \tag{13}$$

where

$$\begin{cases} f^p(r), f^e(r) = 0 & \text{if } 0 \le r \le r_0, \\ f^p(r), f^e(r) > 0 & \text{if } r_0 < r, \end{cases}$$

and r_0 is such that $\Omega_0 = \{(r,\theta,\phi) : 0 \le r < r_0\}$. For convenience, we will denote $\int_0^r f^e(r)dr$ and $\int_0^r f^p(r)dr$ as $F^e(r)$ and $F^p(r)$, respectively. We now express Eqns. (7b), (7c), and (12) in the standard orthonormal spherical basis $\{\boldsymbol{e}_r, \boldsymbol{e}_\theta, \boldsymbol{e}_\phi\}$. The simplest way to compute the Jacobian transformation $\boldsymbol{\Lambda}$ is taking the differentials of position vectors, $\boldsymbol{x} = r\boldsymbol{e}_r$ and $\tilde{\boldsymbol{x}} = \tilde{r}(r)\boldsymbol{e}_r$, using the same basis for $\tilde{\boldsymbol{x}}$. Simple differentiations give the relation:

$$d\tilde{\boldsymbol{x}} = \left[\frac{d\tilde{r}}{dr}\boldsymbol{e}_r\otimes\boldsymbol{e}_r + \frac{\tilde{r}}{r}(\boldsymbol{e}_\theta\otimes\boldsymbol{e}_\theta + \boldsymbol{e}_\phi\otimes\boldsymbol{e}_\phi)\right] d\boldsymbol{x},$$

from which one obtains the Jacobian by Def. (9) as:

$$\boldsymbol{\Lambda} = \frac{d\tilde{r}}{dr}\boldsymbol{e}_r\otimes\boldsymbol{e}_r + \frac{\tilde{r}}{r}(\boldsymbol{e}_\theta\otimes\boldsymbol{e}_\theta + \boldsymbol{e}_\phi\otimes\boldsymbol{e}_\phi). \tag{14}$$

Using relations (13), (14), and (11), Eqns. (12), (7b), and (7c) are combined into the compact equation:

$$(\mathrm{i}\omega)^2\rho\boldsymbol{u}\det\boldsymbol{\Lambda} - \boldsymbol{\nabla}\cdot[\boldsymbol{\sigma} + \boldsymbol{\Sigma}]^T = \boldsymbol{f}\det\boldsymbol{\Lambda}, \tag{15}$$

where $\boldsymbol{\sigma}(\boldsymbol{\nabla u})$ is a conventional stress tensor for elasticity and $\boldsymbol{\Sigma}$ is an *unsymmetric* tensor whose components Σ_{ij} $(i,j = r,\theta,\phi)$ are functions of $\mathrm{i}\omega$ and $(\nabla u)_{kl}$ $(k,l = r,\theta,\phi)$. We note that on Ω_0, $\boldsymbol{\Sigma} = \boldsymbol{0}$ and $\boldsymbol{\Lambda} = \boldsymbol{I}$, the identity tensor. Thus Eqn. (15) reduces to the conventional elastic equation in the part of the domain where we desire the solution. For isotropy the stiffness tensor is given by:

$$\mathsf{C}_{ijkl} = \lambda\delta_{ij}\delta_{kl} + \mu\delta_{ik}\delta_{jl} + \mu\delta_{il}\delta_{jk} \quad i,j,k = r,\theta,\phi. \tag{16}$$

The components of $\boldsymbol{\Sigma}$ in the spherical basis for isotropy in the frequency-domain are given in Appendix A.1.

We now *inverse* transform Eqn. (15) into the time-domain. This requires transforming each component of $\boldsymbol{\Sigma}$ as well as the other $\mathrm{i}\omega$-dependent terms in Eqn. (15), i.e., $\boldsymbol{u}\det\boldsymbol{\Lambda}$ and $\boldsymbol{f}\det\boldsymbol{\Lambda}$. We first note that, since $\boldsymbol{f} = \boldsymbol{0}$ in the PML domain, $\boldsymbol{f}\det\boldsymbol{\Lambda} = \boldsymbol{f}$ holds everywhere and we do not need any special treatment for this term. On the other hand, $\boldsymbol{u}\det\boldsymbol{\Lambda}$ contains $\frac{1}{\mathrm{i}\omega}\boldsymbol{u}$ which results in an inverse transformation integral. This motivates the definition of a vector of auxiliary functions $\boldsymbol{h}$ as:

$$\boldsymbol{h} = \frac{1}{\mathrm{i}\omega}\boldsymbol{u},$$

which permits the inverse transformation of $\Sigma_{ij}(i = \theta,\phi,\ j = r,\theta,\phi)$ as well as $\boldsymbol{u}\det\boldsymbol{\Lambda}$ without the explicit need for inverse transformation integrals. The expressions for $\Sigma_{rj}(j = r,\theta,\phi)$ have yet another factor $1/(\mathrm{i}\omega + C_0)$ which produces convolution integrals upon inverse transformation. Among other possibilities, we define three *additional* auxiliary functions:

$$g_1 = \left(C_2\frac{1}{\mathrm{i}\omega} + C_3\frac{1}{\mathrm{i}\omega + C_0}\frac{1}{\mathrm{i}\omega}\right)(\nabla u)_{rr}, \tag{17a}$$

$$g_2 = \left(C_2\frac{1}{\mathrm{i}\omega} + C_3\frac{1}{\mathrm{i}\omega + C_0}\frac{1}{\mathrm{i}\omega}\right)(\nabla u)_{\theta r}, \tag{17b}$$

$$g_3 = \left(C_2\frac{1}{\mathrm{i}\omega} + C_3\frac{1}{\mathrm{i}\omega + C_0}\frac{1}{\mathrm{i}\omega}\right)(\nabla u)_{\phi r}, \tag{17c}$$

which result in a time-domain system to be solved for $\boldsymbol{u}$, $\boldsymbol{h}$, g_1, g_2, and g_3. Auxiliary equations corresponding to these three additional unknowns are obtained by multiplying both sides of Eqns. (17) by $\mathrm{i}\omega + C_0$ and

inverse-transforming. The resulting problem is summarized as follows. For convenience, we make the system first-order in time by introducing $\boldsymbol{v} = \dot{\boldsymbol{u}}$, resulting in a system of 12 equations for 12 unknowns:

Find $\boldsymbol{u}$, $\boldsymbol{v}$, $\boldsymbol{h}$, g_1, g_2, g_3 on Ω such that:

$$\dot{\boldsymbol{u}} = \boldsymbol{v}, \tag{18a}$$

$$\rho C_4 \dot{\boldsymbol{v}} - \boldsymbol{\nabla}\cdot[\boldsymbol{\sigma} + \boldsymbol{\Sigma}]^T = -\rho\left(C_5\boldsymbol{v} + C_6\boldsymbol{u} + C_7\boldsymbol{h}\right) + \boldsymbol{f}, \tag{18b}$$

$$\dot{\boldsymbol{h}} = \boldsymbol{u}, \tag{18c}$$

$$\dot{g}_1 = -C_0 g_1 + C_2(\nabla u)_{rr} + (C_0C_2 + C_3)(\nabla h)_{rr}, \tag{18d}$$

$$\dot{g}_2 = -C_0 g_2 + C_2(\nabla u)_{\theta r} + (C_0C_2 + C_3)(\nabla h)_{\theta r}, \tag{18e}$$

$$\dot{g}_3 = -C_0 g_3 + C_2(\nabla u)_{\phi r} + (C_0C_2 + C_3)(\nabla h)_{\phi r}, \tag{18f}$$

where

$$\begin{aligned} &\boldsymbol{u} = \bar{\boldsymbol{u}} \quad \text{on } \partial\Omega_u, \\ &\left[\boldsymbol{\sigma} + \boldsymbol{\Sigma}\right]^T \boldsymbol{n} = \boldsymbol{t} \quad \text{on } \partial\Omega_t, \end{aligned}$$

and

$$\begin{aligned} &\boldsymbol{\sigma} = \mathsf{C} : \boldsymbol{\epsilon}, \quad (\mathsf{C} \text{ given in Eqn. (16)}), \\ &\boldsymbol{\epsilon} = \frac{1}{2}\left[\boldsymbol{\nabla u} + \boldsymbol{\nabla u}^T\right]. \end{aligned}$$

$C_0, C_1, \cdots, C_7$ are functions of r but constant in time. Precise expressions are given in Eqns. (27) and (29) and the expressions for $\Sigma_{ij}(i,j = r,\theta,\phi)$, which are obtained by transforming Eqns. (26), are given in Eqns. (28); see Appendix A.2. As is often done in practice we set $\bar{\boldsymbol{u}} = \boldsymbol{0}$ on the outer boundary of the PML.

Since Eqn. (18b) inherits the structure of the conventional elasticity equation, Eqn. (18b) can be readily discretized by standard finite element methods or discontinuous Galerkin methods on unstructured meshes. A boundary integral $\int_\Gamma \boldsymbol{w}[\boldsymbol{\sigma} + \boldsymbol{\Sigma}]^T \boldsymbol{n} d\Gamma$ in a weak formulation of Eqn. (18b) is naturally treated; e.g. on a traction-free boundary of the PML, this term is simply set zero.

Since it is often convenient to resolve system (18) in a standard Cartesian basis $\{\boldsymbol{e}_x, \boldsymbol{e}_y, \boldsymbol{e}_z\}$ for implementational purposes, the components of $\boldsymbol{\Sigma}$ in the spherical basis $\{\boldsymbol{e}_r, \boldsymbol{e}_\theta, \boldsymbol{e}_\phi\}$ should be transformed according to the basis transformation rules between the two frames as well as the components of $\boldsymbol{\nabla u}$, $\boldsymbol{\nabla v}$, and $\boldsymbol{\nabla h}$.

Note that by defining auxiliary functions as in Eqns. (17), one can ensure stability of the system (18) in the case of $f_p, F_p = 0$, since it keeps the structure of the standard second-order formulation of elasticity with real coordinate-stretching. Furthermore, since the auxiliary functions (17) allow for individual inversions of $(\tilde{\nabla} u)_{rr}$, $(\tilde{\nabla} u)_{\theta r}$, and $(\tilde{\nabla} u)_{\phi r}$, and thus $\tilde{\boldsymbol{\sigma}}$ according to Eqns. (7b) and (7c), our PML formulation may find possible applications to anisotropic problems without introducing any additional auxiliary functions.

For axisymmetric problems, the spherical PML formulation above can be reduced to an axisymmetric PML formulation; see Appendix B for details.

3 Discretization

3.1 Spatial discretization

For the numerical discretization of Eqns. (18) or its axisymmetric counterpart (30), we closely follow the procedure presented in [32]. Here we only give a brief description of the methods, mainly emphasizing the differences due to our PML formulation. For further details we refer to [32].

For the spatial discretization of Eqns. (18), we use a second-order discontinuous Galerkin method [33] with numerical fluxes according to the Compact Discontinuous Galerkin (CDG) scheme [34]. Let the computational domain Ω be discretized by a set of non-overlapping elements $\mathcal{T}_h = \{K\}$. Introduce the piecewise

polynomial finite element spaces V_h^p and Σ_h^p:

$$V_h^p = \{\boldsymbol{v} \in \left[L^2(\Omega)\right]^n : |\boldsymbol{v}|_K \in [\mathcal{P}_p(K)]^n \quad \forall K \in \mathcal{T}_h\},$$
$$\Sigma_h^p = \{\boldsymbol{\tau} \in \left[L^2(\Omega)\right]^{n\times m} : |\boldsymbol{\tau}|_K \in [\mathcal{P}_p(K)]^{n\times m} \quad \forall K \in \mathcal{T}_h\},$$

where $\mathcal{P}_p(K)$ is the space of polynomial functions of degree at most $p \geq 1$ on K, $n = 12$ is the number of solution components, and $m = 3$ is the space dimension. We first rewrite Eqns. (18) as a system of first-order equations:

$$\boldsymbol{m}\frac{\partial \boldsymbol{u}}{\partial t} + \boldsymbol{\nabla}\cdot\boldsymbol{F}(\boldsymbol{u},\boldsymbol{H}) = \boldsymbol{S}(\boldsymbol{u},\boldsymbol{H}) + \boldsymbol{f}, \tag{19a}$$
$$\boldsymbol{H} - \boldsymbol{\nabla}\boldsymbol{u} = \boldsymbol{0}, \tag{19b}$$

where (with an abuse of notation) $\boldsymbol{u}$ now represents an array of the unknown functions $\boldsymbol{u}$, $\boldsymbol{v}$, $\boldsymbol{h}$, g_1, g_2, and g_3; $\boldsymbol{m}$, $\boldsymbol{F}$, $\boldsymbol{S}$, and $\boldsymbol{f}$ are tensors representing generalized mass, stresses, sources, and body forces. The finite element formulation is then given as:

Find $\boldsymbol{u}_h \in V_h^p$ and $\boldsymbol{H}_h \in \Sigma_h^p$ such that for all $K \in \mathcal{T}_h$,

$$\int_K \left(\boldsymbol{m}\frac{\partial \boldsymbol{u}_h}{\partial t} - \boldsymbol{S}(\boldsymbol{u_h},\boldsymbol{H}_h)\right)\cdot\boldsymbol{v}d\boldsymbol{x} - \int_K \boldsymbol{F}(\boldsymbol{u_h},\boldsymbol{H}_h) : \nabla\boldsymbol{v}d\boldsymbol{x}$$
$$+ \int_{\partial K} \widehat{\boldsymbol{t}}(\boldsymbol{u}_h,\boldsymbol{H}_h)\cdot\boldsymbol{v}d\boldsymbol{s} = \int_K \boldsymbol{f}\cdot\boldsymbol{v}d\boldsymbol{x}, \quad \forall\boldsymbol{v} \in [\mathcal{P}_p(K)]^n,$$
$$\int_K \boldsymbol{H}_h : \boldsymbol{\tau}d\boldsymbol{x} + \int_K \boldsymbol{u}_h\cdot(\boldsymbol{\nabla}\cdot\boldsymbol{\tau})\,d\boldsymbol{x} - \int_{\partial K}(\widehat{\boldsymbol{u}}_h\otimes\boldsymbol{n}) : \boldsymbol{\tau}d\boldsymbol{s} = \boldsymbol{0}, \quad \forall\boldsymbol{\tau} \in [\mathcal{P}_p(K)]^{n\times m}.$$

We specify appropriate numerical fluxes $\widehat{\boldsymbol{u}}_h$ and $\widehat{\boldsymbol{t}}(\boldsymbol{u}_h,\boldsymbol{H}_h)$ on all element boundaries, eliminate $\boldsymbol{H}_h$ locally from the system, and assemble a semi-discrete system of equations for $\boldsymbol{u}_h$ as:

$$\boldsymbol{M}\frac{d\boldsymbol{U}}{dt} = -\boldsymbol{K}\boldsymbol{U} + \boldsymbol{F}, \tag{20}$$

where $\boldsymbol{U}$ is a vector of nodal variables, $\boldsymbol{M}$ is the mass matrix, $\boldsymbol{K}$ is the stiffness matrix, and $\boldsymbol{F}$ is the force vector. Again the details are given in [32] and thus omitted here. Finally, we set the stabilization parameter of the CDG scheme to $C_{11} = 200/h_{min}$, where h_{min} is the smallest edge length of a triangle/tetrahedron.

The mass matrix $\boldsymbol{M}$ in Eqn. (20) from the DG discretization is block-diagonal and can therefor be explicitly inverted to obtain:

$$\frac{d\boldsymbol{U}}{dt} = -\boldsymbol{M}^{-1}\boldsymbol{K}\boldsymbol{U} + \boldsymbol{M}^{-1}\boldsymbol{F}. \tag{21}$$

This system of ODEs can be integrated numerically for $\boldsymbol{U}$ using any time-integration scheme. Here we use the standard explicit fourth-order Runge-Kutta method.

3.2 Stabilization

We note here that Eqn. (18b) involves first-order spatial derivatives of g_1, g_2, and g_3, and Eqns. (18d), (18e), and (18f) involve first-order derivatives of $\boldsymbol{u}$ and $\boldsymbol{h}$. These terms add an advective character to the PML system, which requires special consideration for the numerical discretization. Existing PML formulations for elasticity have similar equations (see e.g. [19]) but to our knowledge their advective character has attracted little attention. One symptom of advection is numerical instability; for coarse meshes we indeed observe exponential solution growth in time when the PML functions f^e and f^p increase rapidly with r. These instabilities can be removed by refining the mesh or by adding artificial diffusion in the form $-\boldsymbol{\nabla}\cdot\varepsilon\boldsymbol{\nabla}\boldsymbol{v}$ to the left-hand side of Eqn. (18b). Here ε is defined as:

$$\varepsilon = \begin{cases} \varepsilon_0\cos^2\left(\frac{r-r_0}{2\kappa}\pi\right) & \text{if } r_0-\kappa < r < r_0+\kappa, \\ 0 & \text{otherwise,} \end{cases}$$

where $\varepsilon_0 \sim h\omega_0(f^e + f^p)_{max}$ and κ is chosen sufficiently large. Addition of artificial diffusion to the axisymmetric problem (30) is done in an obvious manner.

We observe in our numerical examples that PML functions which provide good accuracy in the sense of small reflection coefficients are long-time stable and artificial diffusion is not needed in such cases. However, on coarser meshes it is required for stability. Many other strategies have been proposed for stabilization of Galerkin formulations, such as upwinded Petrov-Galerkin schemes [35] or modified numerical fluxes in the discontinuous Galerkin formulation. However, we have found that our simple artificial diffusion approach is sufficient for our applications, and produces well-behaved computations on coarse discretizations.

4 Numerical examples

In this section we present several examples in two and three spatial dimensions. We consider an isotropic media with mass density 4.127[Mg/m^3], Young's modulus 139[GPa], and Poisson's ratio 0.28. The domain is discretized using the DistMesh mesh generator [36] for two-dimensional problems, which generates highly regular unstructured triangular meshes, and by netgen for three-dimensional problems utilizing unstructured tetrahedral meshes. For both the two- and the three-dimensional problems, we use the discontinuous Galerkin method with the CDG scheme implemented in the 3DG software package [37] (a general purpose software package for continuous/discontinuous Galerkin methods) for spatial discretization and a fourth order explicit Runge-Kutta method (RK4) for temporal discretization unless otherwise noted.

The PML-complex-transformation functions are assumed to have parabolic profiles:

$$f^p(r) = \beta^p \left(\frac{r - r_0}{r_{pml} - r_0} \right)^2, \quad r_0 < r \leq r_{pml},$$
$$f^e(r) = \beta^e \left(\frac{r - r_0}{r_{pml} - r_0} \right)^2, \quad r_0 < r \leq r_{pml},$$

where β^p and β^e are the values of $f^p(r)$ and $f^e(r)$ on the outer boundary of the PML.

4.1 Axisymmetric problems

4.1.1 Stability study

We first study the stability properties of our PML formulation using an axisymmetric test problem. The setup of the problem is given in Fig. 1a. The edge $R = 0$ is the axis of symmetry. The surface $z = 0$ is traction-free, and a uniform Gaussian pressure pulse

$$f(t) = e^{-\left(\frac{t-\alpha}{w}\right)^2}, \quad \alpha = 6, \quad w = 0.01/f_0, \tag{23}$$

is applied along the inner hole, where we set $f_0 = 0.0613$[GHz] in this example. The average displacement over the entire domain in the R-direction $\bar{u}_R$ is measured up to $T = 10,000$[ns]. Note that the transit time for a P-wave traveling a distance r_0 is about 0.30[ns].

The domain is truncated at $r_0 = 2.0[\mu\text{m}]$ and surrounded by a PML of depth $r_{pml} - r_0 = 1.5[\mu\text{m}]$, modeling an unbounded domain which extends to $r \to +\infty$. The outer boundary of the PML is clamped. Discretization of the domain is performed by DistMesh; see Fig. (1a). The smallest edge length of a triangle h_{min} is set to $h_{min} = 0.50[\mu\text{m}]$, and polynomials of degree $p = 4$ are used. In this example problem, we set $\omega_0 = 4\pi$ and $\beta^e = 0$ and use three different β^p: 4, 400, and 4000. We note that in this setting the optimum β^p in the sense of reflection is estimated as $\beta^p \approx 4$ by our PML parameter choosing heuristics; see Appendix C. Artificial diffusion of $\varepsilon = 1$ is added as needed for stabilization. For simplicity in this example, we use a continuous Galerkin method in space and a trapezoidal method in time. The time-step Δt is set to 1[ns].

Fig. 1b shows plots of $\log_{10} \bar{u}_R$ versus time. Without stabilization, the scheme is stable for $\beta^p = 4$ and 400, but unstable for $\beta^p = 4000$. One can see, however, that addition of artificial diffusion removes this instability. This example demonstrates the ability of artificial diffusion to stabilize our numerical scheme

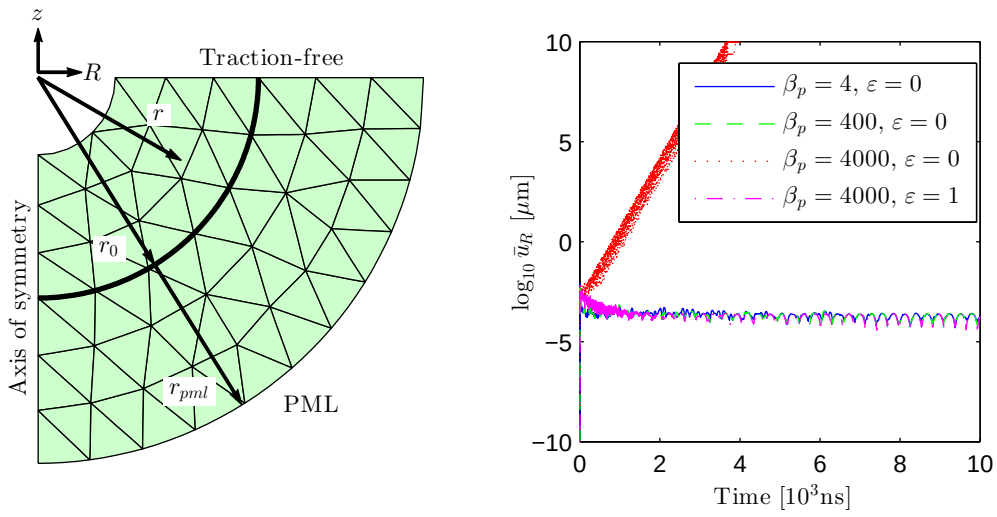

(a) (b)

Figure 1: (a) Problem setup for a stability study. (b) Plots of computed $\bar{u}_R$ versus time on a semi-log scale.

when needed. Though it should be noted that $\beta^p = 4000$ is a very high value and the mesh is exceedingly coarse. When using mesh sizes that provide reasonable accuracy and using *optimal* PML parameters (see Appendix C), we find that stabilization is unnecessary.

4.1.2 Accuracy study

We next validate the accuracy of our proposed axisymmetric PML formulation. The setup of the problem is given in Fig. 2. The edge $R = 0$ is the axis of symmetry. The surface $z = 0$ is traction-free, and uniform Gaussian pressure pulses (23) with $f_0 = 0.0613$[GHz] are applied along the edges of the inner holes, generating a complex wave pattern. The domain is truncated at $r_0 = 8.0[\mu\text{m}]$ and surrounded by a PML of depth $r_{pml} - r_0 = 1.5[\mu\text{m}]$.

The domain is again discretized using DistMesh; see Fig. (2). The smallest edge length of a triangle is set to $h_{min} = 0.50[\mu\text{m}]$ and again fourth-order elements are used.

Considering the nature of the excitation and the discretization, we set $\omega_0 = 4\pi$ and $\beta^p = 4$ based on a one-dimensional parameter study; see Appendix C. We use two different values for β^e, i.e. $\beta^e = 0$ and $\beta^e = 4$, to see its effect on the accuracy.

Finally, we use a fixed time-step of $1 \cdot 10^{-3}$[ns] for time-integration. Displacements in the R- and z-directions are recorded up to 10[ns] at the sensor located right on the PML interface $(R, z) = (r_0, 0)$ as depicted in Fig. 2, which are compared with reference solutions $u_{\text{reference}}$ computed on an extended domain.

Figs. 3a and 3b show plots of computed u_R and u_z against time, respectively, each of which compares four solutions – a reference solution, PML solutions with $(\beta^p, \beta^e) = (4, 0)$ and $(\beta^p, \beta^e) = (4, 4)$, and a solution obtained by applying the classical Lysmer-Kuhlemeyer damper (LK-damper) [38] on $r = r_{pml}$ without any PML elements. The plots clearly demonstrates that both types of PML behave much better than the LK-damper, and show good agreement with the reference solution. Figs. 3c and 3d plot absolute differences between the PML solutions and the reference solutions, where a slight improvement can be observed due to the the additional parameter β^e. The relative errors of the PML solutions are about 0.5%, which we regard as satisfactory considering the complex nature of the problem. We note that the value of the parameter β^e is chosen rather arbitrarily and its optimization has yet to be studied.

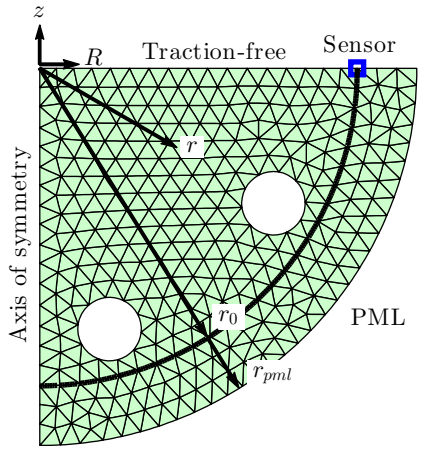

Figure 2: Problem setup for an accuracy study: Hole centers are located at $r = 0.85r_0$ and at angles $\pi/12$ and $\pi/3$ from the vertical.

4.1.3 Axisymmetric resonator

As a final two-dimensional example we test the use of our PML formulation for the computation of the quality factor Q of two MEMS resonators [22, 32]. In the standard approach for computing resonator quality factors, a generic eigenvalue solver is used to directly compute the complex-valued resonant frequencies (eigenvalues) of the system from which the quality factor Q can be computed. However as shown in [32], this is only practical for systems with a relatively small number of degrees of freedom. For full three-dimensional problems, a transient dynamical approach can be shown to scale well, where eigenvalues are extracted from time-series data by filter diagonalization [39]. Good behavior, notwithstanding method, will always rely on a high quality radiation (non-reflecting) boundary condition.

To assess the impact of our PML formulation on this type of problem we consider two axisymmetric resonators as shown in Fig. 4. Resonator A as shown in Fig. 4a has a disk of radius $R_0 = 32[\mu\text{m}]$ attached to a semi-infinite substrate by a cylindrical post of radius $1.0[\mu\text{m}]$ and height $0.70[\mu\text{m}]$. Resonator B as shown in Fig. 4b has an additional mushroom-like structure on top of the disk. Mushroom caps are an artifact of a popular manufacturing process for MEMS resonators [1, 40]. In our case, the modeled cap has radius $6.5[\mu\text{m}]$ and thickness $2.0[\mu\text{m}]$ and sits on a post of radius $1.0[\mu\text{m}]$ and height $1.0[\mu\text{m}]$. The thickness of the $32[\mu\text{m}]$ disk varies from $1.2[\mu\text{m}]$ to $1.8[\mu\text{m}]$ and the sensitivity of the quality factors to the thickness variation is studied. The surfaces of these resonators are assumed to be traction-free. Each semi-infinite substrate is truncated at radius $r_0 = 8.0[\mu\text{m}]$ and a PML of depth $r_{pml} - r_0 = 1.5[\mu\text{m}]$ is attached surrounding the resulting finite domain. As before, unstructured triangular meshes are generated by DistMesh with $h_{min} = 0.50[\mu\text{m}]$ and element orders of 4 as shown in Fig. 4. We set $\omega_0 = 4\pi$ and $(\beta^p, \beta^e) = (4, 4)$ for the PML parameters.

The quality factor corresponding to a mode with eigenvalue $\mathrm{i}\omega$ is defined as:

$$Q = \frac{|\omega|}{2\text{Im}\,(\omega)}. \tag{24}$$

The fundamental angular frequency ω^* of the disks can be estimated as [41]:

$$\omega^*_{\text{estimate}} = 2.04\frac{c_0}{R_d} \tag{25}$$

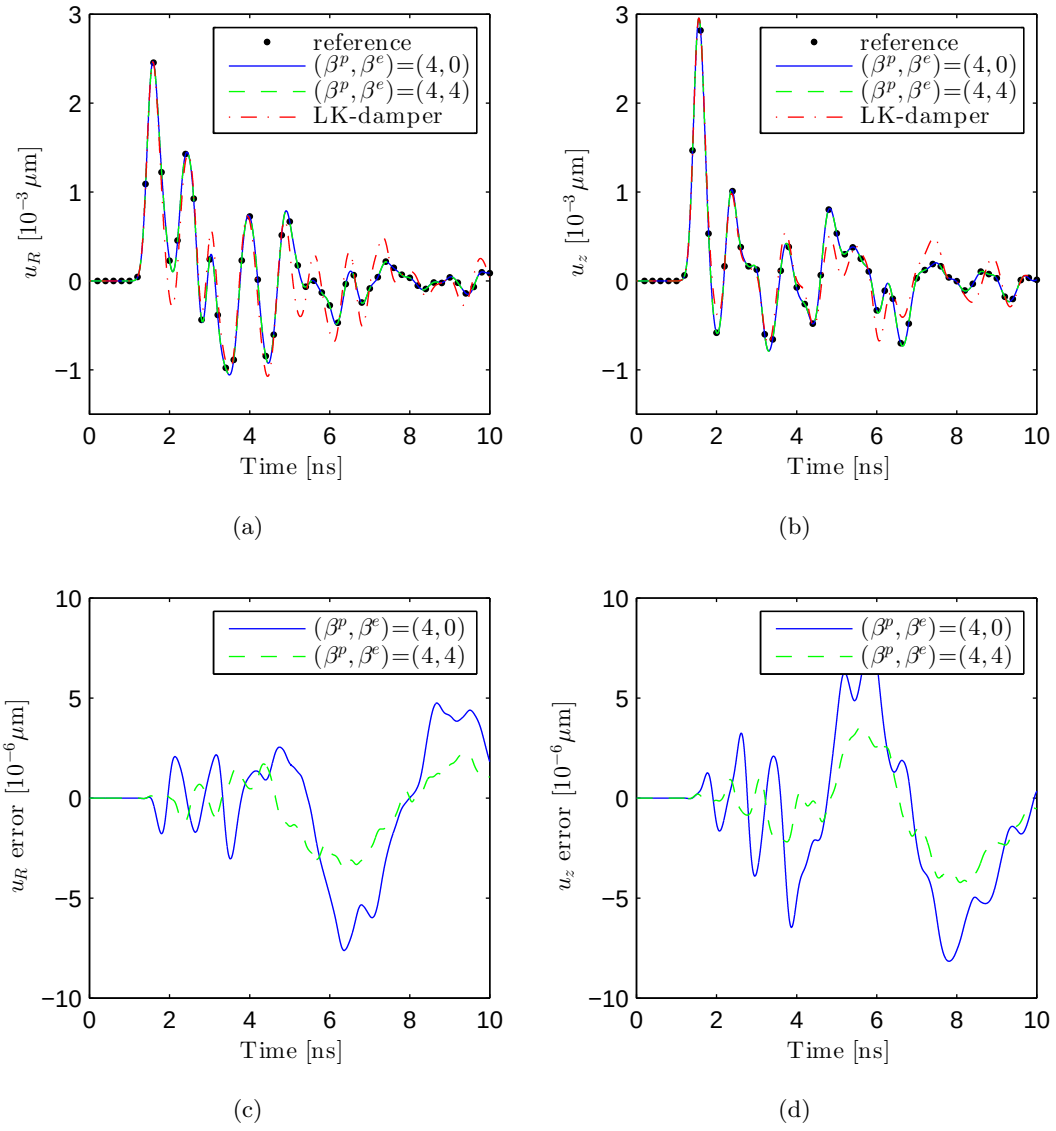

Figure 3: Plots of computed (a) u_R and (b) u_z versus time for four solutions and absolute differences of the PML solutions (c) u_R and (d) u_z from the reference solutions.

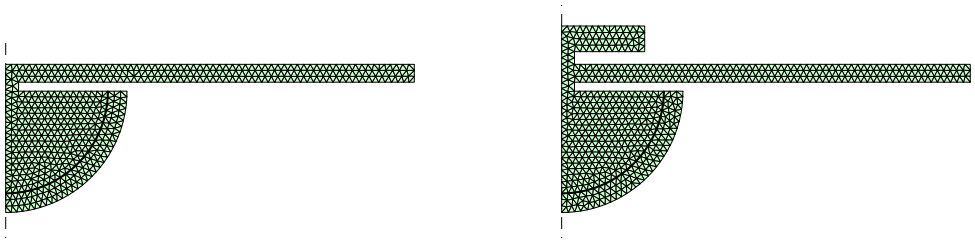

(a) Resonator A (b) Resonator B

Figure 4: Geometry and triangular mesh of (a) a resonator with flat top (b) a resonator with mushroom-like structure.

where $c_0 = 6.045[\mu\text{m/ns}]$ is the plane-stress radial wave speed. We thus find an eigenvalue of $\boldsymbol{M}^{-1}\boldsymbol{K}$ in the semi-discrete system (21) whose imaginary part is closest to $\mathrm{i}\omega^*_{\text{estimate}}$ and compute the corresponding quality factor using Def. (24) for various film-thicknesses between 1.2 and 1.8[μm]. We first compute eigenvalues directly using a generic eigenvalue solver. Plots of quality factor versus film-thickness are shown in solid and dashed lines in Fig. 5a for resonators A and B, respectively. Note that resonator A exhibits a wild swing in Q around a thickness of 1.48[μm], while resonator B shows little sensitivity to the thickness of the film.

Direct eigenvalue computation, however, is only applicable to a small system due to its high memory requirements. In [32] an alternative transient methodology to compute the quality factors of the fundamental modes was proposed and its accuracy and scalability were demonstrated through three-dimensional problems of resonators using LK-dampers. For later application of our PML formulation to full three-dimensional resonator problems, we also adopt the methodology presented in [32] to our axisymmetric resonator problems to compute the quality factors. Specifically, we apply a broadband Gaussian pulse (23) with $f_0 = \omega^*_{\text{estimate}}/2\pi$ radially on the edge of the disk, solve system (21) using a fourth-order explicit Runge-Kutta method with $\Delta t = 1 \cdot 10^{-3}$[ns] up to $5,000$[ns], and record a time-series of average radial displacement $\bar{u}_R$ over the entire domain. Next a *filter diagonalization method* [39] is applied to this time-series data using the harminv software [42], which extracts for each excited mode its frequency, rate of damping, and quality factor. We pick the quality factor corresponding to a mode whose frequency is closest to $\omega^*_{\text{estimate}}$. In using harminv, we cut off the first 10[ns] of the time-series, store data at every 200th time-step, and specify a broad range of frequencies 10^{-4}-10^{4}[GHz] over which we expect to find the fundamental mode. Quality factors thus obtained are plotted in Fig. 5a as black dots, which show good agreement with values obtained by the eigenvalue solver. Fig. 5b shows relative errors of quality factors computed by harminv compared to the ones obtained by exact eigenvalue analysis. We note that experimental data shows such wild swings in flat top resonators [2] and that experience shows these swings are absent in resonators with mushroom caps [43].

4.2 Three-dimensional problems

One of the main impetuses for the development of our spherical PML formulation was the accurate simulation of three-dimensional resonator systems where eigenvalue extraction is only feasible via time-series analysis coupled to filter diagonalization [39, 32]. In this setting computational cost reduction is of paramount importance. In this section we look at the numerical properties of our proposed method as well as demonstrate its use on a large scale problem.

4.2.1 Convergence study

First, we validate the spatial and temporal convergence rates of our DG formulation in conjunction with a RK4 time-integrator for three-dimensional problems. We consider a hollow sphere with inner and outer radii of 1.0 and 2.0, respectively, which has material properties of $\lambda = 1.0$, $\mu = 1.0$, and $\rho = 3.0$. The inner boundary is clamped and the outer boundary is traction-free. As output quantity for the error calculation,

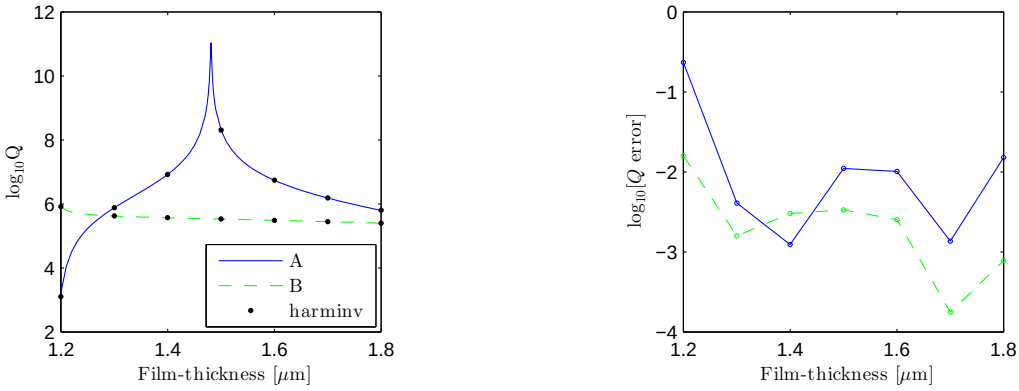

(a) (b)

Figure 5: Plots of (a) $\log_{10} Q$ computed by an eigenvalue solver and harmonic inversion and (b) relative errors of Q computed by harmonic inversion compared to that computed by an eigenvalue solver for various film thicknesses for Resonator A and Resonator B.

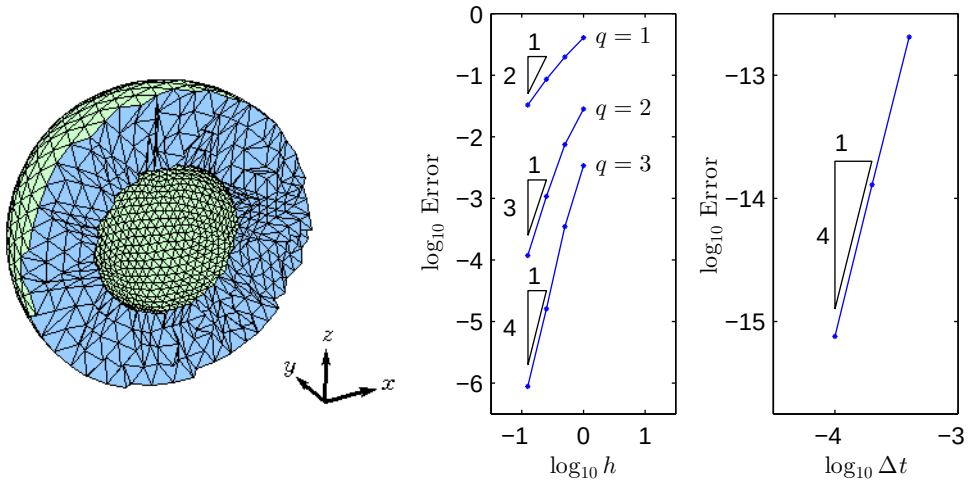

(a) (b) (c)

Figure 6: (a) Problem setup for a convergence study. Plots of error versus (b) h and (c) Δt in log-log scale.

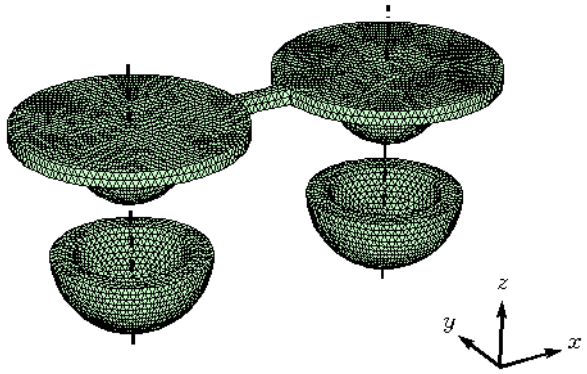

Figure 7: The double-disk resonator with its semi-infinite substrate replaced by the PML-bowls. A tetrahedral mesh is also shown.

we study the average x-displacement $\bar{u}_x$ on the outer boundary.

To demonstrate the spatial convergence, we compute steady-state displacements of the hollow sphere subject to a body-force of $\boldsymbol{f} = (e^z, 0, 0)^T$. A sequence of uniformly refined unstructured meshes and polynomial degrees of $q = 1, ..., 4$ are used. The coarsest mesh has a single layer of tetrahedral elements across the thickness and a total of 381 tetrahedra. We refer to this element-size as $h = 1$. Each tetrahedron is then repeatedly split into 8 similar tetrahedra to produce a sequence of meshes of element-sizes $h_r = 1/2^r$, $r = 0, ..., 4$. Fig. 6a shows an example mesh corresponding to $r = 2$ generated by netgen. Considering the output quantity corresponding to $h_4 = 1/16$ and $q = 4$ as the "exact solution" $\bar{u}_{x,\text{exact}}$, errors $|\bar{u}_x - \bar{u}_{x,\text{exact}}|$ are computed for $q = 1, 2, 3$ and plotted in Fig. 6b against element-size h on a log-log scale. We note that the slopes are close to the expected $q + 1$ order of convergence.

To confirm the expected temporal convergence rate, we consider the mesh of $r = 4$ and $q = 4$. We multiply the body-forces by a smooth Gaussian profile in time:

$$\boldsymbol{b}(t) = \left(e^{-\left(\frac{t-0.1}{0.01}\right)^2} e^z, 0, 0\right)^T$$

and integrate until time $T = 1$ using four different time-steps $\Delta t = 4 \cdot 10^{-4}/2^s$ $s = 0, ..., 3$. The solution corresponding to the finest time-step is considered as "exact". Fig. 6c shows plots of errors at $T = 1$ against time-step Δt on a log-log scale and we can observe the expected fourth-order rate of convergence for the error.

4.2.2 Double-disk resonator

As our last example we compute the quality factor of a full three-dimensional double-disk resonator which is anchored to a semi-infinite substrate. Each disk has a radius of $R_d = 8.0[\mu\text{m}]$ and a thickness of $1.1[\mu\text{m}]$ and is anchored to the substrate by a cylindrical post which has a radius of $1.0[\mu\text{m}]$ and a height of $0.50[\mu\text{m}]$. These two disks are separated from each other by $20[\mu\text{m}]$ in the x-direction and connected by a bar with a width of $1.0[\mu\text{m}]$ and a height of $1.1[\mu\text{m}]$. The material properties are the same as were used for the axisymmetric resonator example.

To analyze this problem on a finite domain, we truncate the unbounded substrate and attach PMLs. In this type of problems, our spherical PML shows several advantages over other existing PMLs. First, the

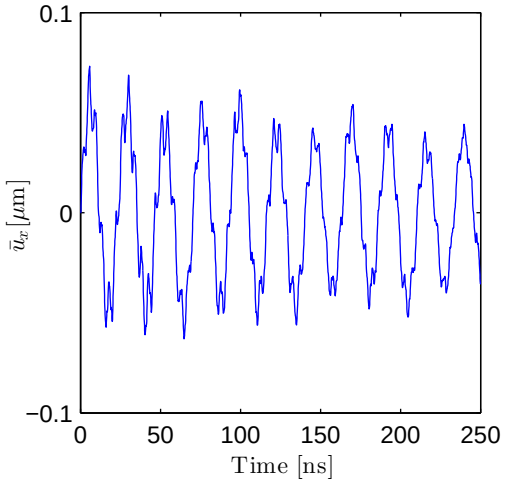

Figure 8: Plots of computed $\bar{u}_R$ versus time for the double-disk resonator problem.

system does not allow for structured meshes, so PML formulations that work with finite element methods on unstructured meshes are required. Existing formulations which do work with finite element methods, however, introduce a large number of nodal variables, which adds significant computational cost for large three-dimensional problems. For instance, the formulation proposed in [27] requires about 2.5 times more memory storage for the PML domains than our formulation. Moreover, while most formulations are based on Cartesian PMLs, spherical PMLs better match this type of problems since resonating disks emit elastic waves almost spherically into the substrate via the small cylindrical posts. Finally, the existence of edges and corners as would be required for Cartesian based PMLs would add significant complexity to the implementation.

Here, the substrate is truncated to leave half spheres of radii 4.0[μm] and "*PML-bowls*" of thickness 1.5[μm] are attached on the surfaces of truncation; see Fig. 7. The outer boundaries of the PML-bowls are clamped and other boundaries are traction-free.

To compute the quality factor of this resonator, we employ the transient dynamical approach introduced in Sec. 4.1.3. The estimate of the fundamental frequency $\omega^*_{\text{estimate}}$ is computed using Eqn. (25) as 1.541×10^9[rad/s]. We apply a Gaussian pulse (23) with $f_0 = \omega^*_{\text{estimate}}/2\pi$ uniformly along the edge of the left disk and record a time-series of the average displacement in the x-direction over the entire domain $\bar{u}_x$ up to 250[ns]. We then apply harmonic-inversion via filter-diagonalization to this time-series via harminv and extract the eigenvalue corresponding to the fundamental radial mode of vibration.

We use netgen to construct an uniform tetrahedral mesh with $h \approx 0.50$[μm]; see Fig. 7. It produces a total of 55,644 elements among which 24,888 are in the PML, which for our polynomial degree of 3 gives about 9.7 million dofs. We set $\Delta t = 8 \cdot 10^{-4}$[ns] to satisfy the CFL-condition. The same set of PML-parameters is used as in Sec. 4.1.3 since the nature of the problem is similar.

Fig. 8 shows a time-series of $\bar{u}_x$. In using harminv, we cut off the first 1[ns] of the time-series, store data at every 125th time-step, and specify a broad range of frequencies 10^{-4}-10^4[GHz]. The resulting eigenvalue $-0.003879 + 1.529\mathrm{i}$ corresponds to a quality factor of $Q = 197.0$. This example problem demonstrates the applicability of our spherical PML to a full real-world three-dimensional problem.

5 Conclusion

A new PML formulation was developed for time-domain analysis of elastic waves on three-dimensional spherical domains or two-dimensional axisymmetric domains. Since our spherical PML formulation is developed based on the regular second-order elastic equation instead of the first-order velocity-stress system, it readily

works with standard finite element methods as well as discontinuous Galerkin methods on unstructured meshes. It is monolithic and simple to implement; it involves no edges or corners as in existing time-domain formulations of Cartesian PMLs which require special treatment. It also allows for a natural application of traction-free boundary conditions, taking advantage of the second-order formulation which is well-suited for elastodynamics. Furthermore, our formulation requires a smaller number of variables than other existing formulations, which is an advantage when solving large three-dimensional problems where memory-usage can be demanding. The formulation was demonstrated using high-order Discontinuous Galerkin discretizations with a CDG scheme on unstructured meshes and a fourth-order explicit Runge-Kutta time-integrator, which showed the high accuracy of the method as well as its ability to solve large three-dimensional problems. Finally, we were able to successfully apply our methods to a large scale resonator problem and extract "damped" eigenvalues using explicit time-integration and a harmonic-inversion technique.

Acknowledgment

This material is based upon work supported by the National Science Foundation under Award No. CMMI-0928785, by the Air Force Office of Scientific Research, USAF, under grant/contract number FA9550-10-1-0229, and by the Director, Office of Science, Computational and Technology Research, U.S. Department of Energy under Contract No. DE-AC02-05CH11231.

References

[1] Wang J, Butler J, Feygelson T, Nguyen CTC. 1.51-GHz polydiamond micromechanical disk resonator with impedance-mismatched isolating support. *Proceedings IEEE International MEMS Conference*, 2004; 641–644.

[2] Bindel DS, Quévy E, Koyama T, Govindjee S, Demmel J, Howe R. Anchor loss simulation in resonators. *Proceedings of MEMS 2005*, IEEE, 2005; 133–136.

[3] Li SS, Lin YW, Ren Z, Nguyen CTC. An MSI micromechanical differential disk-array filter. *Digest of Technical Papers, the 14th International Conference on Solid-State Sensors & Actuators (Transducers '07)*, 2007; 307–311.

[4] Berenger JP. A perfectly matched layer for the absorption of electromagnetic waves. *Journal of Computational Physics* 1994; **114**:185–200.

[5] Chew W, Weedon W. A 3D perfectly matched medium from modified Maxwell's equations with stretched coordinates. *Microwave and Optical Technology Letters* 1994; **7**:599–604.

[6] Chew W, Liu Q. Perfectly matched layers for elastodynamics: A new absorbing boundary condition. *Journal of Computational Acoustics* 1996; **4**:341–359.

[7] Liu Q. Perfectly matched layers for elastic waves in cylindrical and spherical coordinates. *Journal of the Acoustical Society of America* 1999; **105**:2075–2084.

[8] Collino F, Tsogka C. Application of the perfectly matched absorbing layer model to the linear elastodynamic problem in anisotropic heterogeneous media. *Geophysics* 2001; **66**:294–307.

[9] Marcinkovich C, Olsen K. On the implementation of perfectly matched layers in a three-dimensional fourth-order velocity-stress finite difference scheme. *Journal of Geophysical Research* 2003; **108**:2276.

[10] Kuzuoglu M, Mittra R. Frequency dependence of the constitutive parameters of causal perfectly matched anisotropic absorbers. *IEEE Microwave and Guided Wave Letters* 1996; **6**:447–449.

[11] Roden J, Gedney S. Convolution PML (CPML): An efficient FDTD implementation of the CFS-PML for arbitrary media. *Microwave and Optical Technology Letters* 2000; **27**:334–339.

[12] Luebbers R, Hunsberger F. FDTD for Nth-order dispersive media. *IEEE Transactions on Antennas and Propagation* 1992; **40**:1297–1301.

[13] Drossaert F, Giannopoulos A. Complex frequency shifted convolution PML for FDTD modelling of elastic waves. *Wave Motion* 2007; **44**:593–604.

[14] Komatitsch D, Martin R. An unsplit convolutional perfectly matched layer improved at grazing incidence for the seismic wave equation. *Geophysics* 2007; **72**:SM155–SM167.

[15] Martin R, Komatitsch D. An unsplit convolutional perfectly matched layer technique improved at grazing incidence for the viscoelastic wave equation. *Geophysical Journal International* 2009; **179**:333–344.

[16] Ramadan O. Auxiliary differential equation formulation: an efficient implementation of the perfectly matched layer. *IEEE Microwave and Wireless Components Letters* 2003; **13**:69–71.

[17] Gedney S, Zhao B. An Auxiliary Differential Equation Formulation for the Complex-Frequency Shifted PML. *IEEE Transactions on Antennas and Propagation* 2010; **58**:838–847.

[18] Zhen Q, Minghui L, Xiaodong Z, Yao Y, Cai Z, Jianyong S. The implementation of an improved NPML absorbing boundary condition in elastic wave modeling. *Applied Geophysics* 2009; **6**:113–121.

[19] Martin R, Komatitsch D, Gedney S, Bruthiaux E. A High-Order Time and Space Formulation of the Unsplit Perfectly Matched Layer for the Seismic Wave Equation Using Auxiliary Differential Equations (ADE-PML). *Computer Modeling in Engineering & Sciences* 2010; **56**:17–41.

[20] Zhang W, Shen Y. Unsplit complex frequency-shifted PML implementation using auxiliary differential equations for seismic wave modeling. *Geophysics* 2010; **75**:T141–T154.

[21] Basu U, Chopra A. Perfectly matched layers for time-harmonic elastodynamics of unbounded domains: theory and finite-element implementation. *Computer Methods in Applied Mechanics and Engineering* 2003; **192**:1337–1375.

[22] Bindel D, Govindjee S. Elastic PMLs for resonator anchor loss simulation. *International Journal for Numerical Methods in Engineering* 2005; **64**:789–818.

[23] Komatitsch D, Tromp J. A perfectly matched layer absorbing boundary condition for the second-order seismic wave equation. *Geophysical Journal International* 2003; **154**:146–153.

[24] Cohen G, Fauqueux S. Mixed Spectral Finite Elements for the Linear Elasticity System in Unbounded Domains. *SIAM Journal on Scientific Computing* 2005; **26**:864–884.

[25] Festa G, Vilotte JP. The Newmark scheme as velocity-stress time-staggering: an efficient PML implementation for spectral element simulations of elastodynamics. *Geophysical Journal International* 2005; **161**:789–812.

[26] Basu U, Chopra A. Perfectly matched layers for transient elastodynamics of unboundeddomains. *International Journal for Numerical Methods in Engineering* 2004; **59**:1039–1074.

[27] Basu U. Explicit finite element perfectly matched layer for transient three-dimensional elastic waves. *International Journal for Numerical Methods in Engineering* 2009; **77**:151–176.

[28] Li Y, Matar O. Convolutional perfectly matched layer for elastic second-order wave equation. *Journal of the Acoustical Society of America* 2010; **127**:1318–1327.

[29] Kucukcoban S, Kallivokas L. A Mixed Perfectly-Matched-Layer for Transient Wave Simulations in Axisymmetric Elastic Media. *Computer Modeling in Engineering & Sciences* 2010; **64**:109–145.

[30] Kucukcoban S, Kallivokas L. Mixed perfectly-matched-layers for direct transient analysis in 2D elastic heterogeneous media. *Computer Methods in Applied Mechanics and Engineering* 2011; **200**:57–76.

[31] Graff K. *Wave Motion In Elastic Solids*. Dover Publications, Inc., New York, 1991.

[32] Govindjee S, Persson PO. A time-domain Discontinuous Galerkin method for mechanical resonator quality factor computations. *Journal of Computational Physics* 2012; **231**:6380–6392.

[33] Cockburn B, Shu CW. Runge-Kutta discontinuous Galerkin methods for convection-dominated problems. *J. Sci. Comput.* 2001; **16**(3):173–261.

[34] Peraire J, Persson PO. The Compact Discontinuous Galerkin (CDG) Method for Elliptic Problems. *SIAM Journal on Scientific Computing* 2008; **30**:1806–1824.

[35] Brooks AN, Hughes TJR. Streamline upwind/Petrov-Galerkin formulations for convection dominated flows with particular emphasis on the incompressible Navier-Stokes equations. *Comput. Methods Appl. Mech. Engrg.* 1982; **32**(1-3):199–259. FENOMECH '81, Part I (Stuttgart, 1981).

[36] Persson PO, Strang G. A Simple Mesh Generator in Matlab. *SIAM Review* 2004; **46**:329–345.

[37] Peraire J, Persson PO. *Adaptive High-order methods in computational fluid dynamics*, vol. 2. World Scientific Publishing Co., 2011.

[38] Lysmer J, Kuhlmeyer R. Finite dynamic model for infinite media. *J Eng Mech Div ASCE* 1969; **95**:859–877.

[39] Mandelshtam V, Taylor H. Harmonic inversion of time signals and its applications. *Journal of Chemical Physics* 1997; **107**:6756–6769.

[40] Nguyen CTC. MEMS Technology for timing and frequency control. *IEEE Transactions on Ultrasonics, Ferrorelectrics, and Frequency Control* 2007; **54**:251–270.

[41] Govindjee S. Estimation of the fundamental mode of a radial-disk resonator. *Technical Report UCB/SEMM-2011/02*, University of California Berkeley, Department of Civil Engineering 2011.

[42] Johnson S. Harminv (ver. 1.3.1) 2004. URL `http://ab-initio.mit.edu/wiki/indep.php/Harminv`.

[43] Nguyen CTC. 2013. Private communication.

[44] Koyama T. Efficient Evaluation of Damping in Resonant MEMS. PhD Thesis, University of California, Berkeley 2008.

A Tensor components and constants

A.1 Frequency-domain formulation

In the frequency-domain, the components of $\mathbf{\Sigma}$ in Eqn. (15) in the spherical basis $\{\boldsymbol{e}_r, \boldsymbol{e}_\theta, \boldsymbol{e}_\phi\}$ are given by:

$$\begin{aligned}
\Sigma_{rr} &= (\lambda+2\mu)\left(C_1 + C_2\frac{1}{\mathrm{i}\omega} + C_3\frac{1}{\mathrm{i}\omega+C_0}\frac{1}{\mathrm{i}\omega}\right)(\nabla u)_{rr} \\
&\quad + \lambda\left(\frac{F^e}{r} + \frac{\omega_0 F^p}{r}\frac{1}{\mathrm{i}\omega}\right)\left[(\nabla u)_{\theta\theta} + (\nabla u)_{\phi\phi}\right], && \text{(26a)} \\
\Sigma_{r\theta} &= \mu\left(C_1 + C_2\frac{1}{\mathrm{i}\omega} + C_3\frac{1}{\mathrm{i}\omega+C_0}\frac{1}{\mathrm{i}\omega}\right)(\nabla u)_{\theta r} \\
&\quad + \mu\left(\frac{F^e}{r} + \frac{\omega_0 F^p}{r}\frac{1}{\mathrm{i}\omega}\right)(\nabla u)_{r\theta}, && \text{(26b)} \\
\Sigma_{r\phi} &= \mu\left(C_1 + C_2\frac{1}{\mathrm{i}\omega} + C_3\frac{1}{\mathrm{i}\omega+C_0}\frac{1}{\mathrm{i}\omega}\right)(\nabla u)_{\phi r} \\
&\quad + \mu\left(\frac{F^e}{r} + \frac{\omega_0 F^p}{r}\frac{1}{\mathrm{i}\omega}\right)(\nabla u)_{r\phi}, && \text{(26c)} \\
\Sigma_{\theta r} &= \mu\left(f^e + \omega_0 f^p\frac{1}{\mathrm{i}\omega}\right)(\nabla u)_{r\theta} + \mu\left(\frac{F^e}{r} + \frac{\omega_0 F^p}{r}\frac{1}{\mathrm{i}\omega}\right)(\nabla u)_{\theta r}, && \text{(26d)} \\
\Sigma_{\theta\theta} &= \lambda\left(\frac{F^e}{r} + \frac{\omega_0 F^p}{r}\frac{1}{\mathrm{i}\omega}\right)(\nabla u)_{rr} + \lambda\left(f^e + \omega_0 f^p\frac{1}{\mathrm{i}\omega}\right)(\nabla u)_{\phi\phi} \\
&\quad + (\lambda+2\mu)\left(f^e + \omega_0 f^p\frac{1}{\mathrm{i}\omega}\right)(\nabla u)_{\theta\theta}, && \text{(26e)} \\
\Sigma_{\theta\phi} &= \mu\left(f^e + \omega_0 f^p\frac{1}{\mathrm{i}\omega}\right)\left[(\nabla u)_{\theta\phi} + (\nabla u)_{\phi\theta}\right], && \text{(26f)} \\
\Sigma_{\phi r} &= \mu\left(f^e + \omega_0 f^p\frac{1}{\mathrm{i}\omega}\right)(\nabla u)_{r\phi} + \mu\left(\frac{F^e}{r} + \frac{\omega_0 F^p}{r}\frac{1}{\mathrm{i}\omega}\right)(\nabla u)_{\phi r}, && \text{(26g)} \\
\Sigma_{\phi\theta} &= \mu\left(f^e + \omega_0 f^p\frac{1}{\mathrm{i}\omega}\right)\left[(\nabla u)_{\theta\phi} + (\nabla u)_{\phi\theta}\right], && \text{(26h)} \\
\Sigma_{\phi\phi} &= \lambda\left(\frac{F^e}{r} + \frac{\omega_0 F^p}{r}\frac{1}{\mathrm{i}\omega}\right)(\nabla u)_{rr} + \lambda\left(f^e + \omega_0 f^p\frac{1}{\mathrm{i}\omega}\right)(\nabla u)_{\theta\theta} \\
&\quad + (\lambda+2\mu)\left(f^e + \omega_0 f^p\frac{1}{\mathrm{i}\omega}\right)(\nabla u)_{\phi\phi}, && \text{(26i)}
\end{aligned}$$

where C_0, C_1, C_2, and C_3 are temporally constant and defined as:

$$\begin{aligned}
C_0 &= \frac{\omega_0 f^p}{1+f^e}, && \text{(27a)} \\
C_1 &= \frac{\left(1+\frac{F^e}{r}\right)^2}{1+f^e} - 1, && \text{(27b)} \\
C_2 &= \frac{\left(1+\frac{F^e}{r}\right)^2}{1+f^e}\left(\frac{2\frac{\omega_0 F^p}{r}}{1+\frac{F^e}{r}} - C_0\right), && \text{(27c)} \\
C_3 &= \frac{\left(1+\frac{F^e}{r}\right)^2}{1+f^e}\left(\frac{\frac{\omega_0 F^p}{r}}{1+\frac{F^e}{r}} - C_0\right)^2. && \text{(27d)}
\end{aligned}$$

A.2 Time-domain formulation

In the time-domain, the components of $\boldsymbol{\Sigma}$ in Eqn. (18b) in the spherical basis $\{\boldsymbol{e}_r, \boldsymbol{e}_\theta, \boldsymbol{e}_\phi\}$ are given by:

$$\Sigma_{rr} = (\lambda+2\mu)C_1(\nabla u)_{rr} + (\lambda+2\mu)g_1 + \lambda\left(\frac{F^e}{r}\left[(\nabla u)_{\theta\theta} + (\nabla u)_{\phi\phi}\right] + \frac{\omega_0 F^p}{r}\left[(\nabla h)_{\theta\theta} + (\nabla h)_{\phi\phi}\right]\right), \tag{28a}$$

$$\Sigma_{r\theta} = \mu C_1(\nabla u)_{\theta r} + \mu\left(\frac{F^e}{r}(\nabla u)_{r\theta} + \frac{\omega_0 F^p}{r}(\nabla h)_{r\theta}\right) + \mu g_2, \tag{28b}$$

$$\Sigma_{r\phi} = \mu C_1(\nabla u)_{\phi r} + \mu\left(\frac{F^e}{r}(\nabla u)_{r\phi} + \frac{\omega_0 F^p}{r}(\nabla h)_{r\phi}\right) + \mu g_3, \tag{28c}$$

$$\Sigma_{\theta r} = \mu\left(f^e(\nabla u)_{r\theta} + \omega_0 f^p(\nabla h)_{r\theta} + \frac{F^e}{r}(\nabla u)_{\theta r} + \frac{\omega_0 F^p}{r}(\nabla h)_{\theta r}\right), \tag{28d}$$

$$\Sigma_{\theta\theta} = \lambda\left(\frac{F^e}{r}(\nabla u)_{rr} + \frac{\omega_0 F^p}{r}(\nabla h)_{rr} + f^e(\nabla u)_{\phi\phi} + \omega_0 f^p(\nabla h)_{\phi\phi}\right) + (\lambda+2\mu)\left(f^e(\nabla u)_{\theta\theta} + \omega_0 f^p(\nabla h)_{\theta\theta}\right), \tag{28e}$$

$$\Sigma_{\theta\phi} = \mu\left(f^e\left[(\nabla u)_{\theta\phi} + (\nabla u)_{\phi\theta}\right] + \omega_0 f^p\left[(\nabla h)_{\theta\phi} + (\nabla h)_{\phi\theta}\right]\right), \tag{28f}$$

$$\Sigma_{\phi r} = \mu\left(f^e(\nabla u)_{r\phi} + \omega_0 f^p(\nabla h)_{r\phi}\right) + \mu\left(\frac{F^e}{r}(\nabla u)_{\phi r} + \frac{\omega_0 F^p}{r}(\nabla h)_{\phi r}\right), \tag{28g}$$

$$\Sigma_{\phi\theta} = \mu\left(f^e\left[(\nabla u)_{\theta\phi} + (\nabla u)_{\phi\theta}\right] + \omega_0 f^p\left[(\nabla h)_{\theta\phi} + (\nabla h)_{\phi\theta}\right]\right), \tag{28h}$$

$$\Sigma_{\phi\phi} = \lambda\left(\frac{F^e}{r}(\nabla u)_{rr} + \frac{\omega_0 F^p}{r}(\nabla h)_{rr}\right) + \lambda\left(f^e(\nabla u)_{\theta\theta} + \omega_0 f^p(\nabla h)_{\theta\theta}\right) + (\lambda+2\mu)\left(f^e(\nabla u)_{\phi\phi} + \omega_0 f^p(\nabla h)_{\phi\phi}\right), \tag{28i}$$

where g_1, g_2, and g_3 are auxiliary functions defined in Eqns. (18d)-(18f).

Also, the temporal constants C_4, C_5, C_6, and C_7 introduced in Eqns. (18) are defined as:

$$C_4 = (1+f^e)\left(1+\frac{F^e}{r}\right)^2, \tag{29a}$$

$$C_5 = \left(1+\frac{F^e}{r}\right)\left(\omega_0 f^p\left(1+\frac{F^e}{r}\right) + 2\left(1+f^e\right)\frac{\omega_0 F^p}{r}\right), \tag{29b}$$

$$C_6 = \frac{\omega_0 F^p}{r}\left(2\omega_0 f^p\left(1+\frac{F^e}{r}\right) + \left(1+f^e\right)\frac{\omega_0 F^p}{r}\right), \tag{29c}$$

$$C_7 = \omega_0 f^p\left(\frac{\omega_0 F^p}{r}\right)^2. \tag{29d}$$

B Axisymmetric PML

In this section, we present an axisymmetric formulation of our spherical PML. If the problem is axisymmetric, one can set $u_\phi = 0$ and $\frac{\partial}{\partial\phi}(\cdot) = 0$ in the spherical problem (18). Then all $r\phi$-, ϕr-, $\theta\phi$-, and $\phi\theta$-components of $\boldsymbol{\nabla u}$, $\boldsymbol{\nabla v}$, and $\boldsymbol{\nabla h}$, and thus $\boldsymbol{\sigma}$ and $\boldsymbol{\Sigma}$, vanish. It is convenient to resolve problem (18) in the standard cylindrical coordinate system (R, z, ϕ) with the orthonormal cylindrical basis $\{\boldsymbol{e}_R, \boldsymbol{e}_z, \boldsymbol{e}_\phi\}$, where one finds that $R\phi$-, ϕR-, $z\phi$-, and ϕz- components of $\boldsymbol{\nabla u}$ etc. are zero. Then, one is left with 8 non-trivial equations

for 8 unknowns:

$$
\begin{aligned}
&\text{Find } u_R,\ u_z,\ v_R,\ v_z,\ h_R,\ h_z,\ g_1,\ g_2 \text{ on } \Omega \text{ such that:}\\
&\dot{u}_R = v_R, && \text{(30a)}\\
&\dot{u}_z = v_z, && \text{(30b)}\\
&\rho R C_4 \dot{v}_R - [\{R\,(\sigma_{RR} + \Sigma_{RR})\}_{,R} + \{R\,(\sigma_{zR} + \Sigma_{zR})\}_{,z}]\\
&\quad = -\rho R\,(C_5 v_R + C_6 u_R + C_7 h_R) - (\sigma_{\phi\phi} + \Sigma_{\phi\phi})\,, && \text{(30c)}\\
&\rho R C_4 \dot{v}_z - [\{R\,(\sigma_{Rz} + \Sigma_{Rz})\}_{,R} + \{R\,(\sigma_{zz} + \Sigma_{zz})\}_{,z}]\\
&\quad = -\rho R\,(C_5 v_z + C_6 u_z + C_7 h_z)\,, && \text{(30d)}\\
&\dot{h}_R = u_R, && \text{(30e)}\\
&\dot{h}_z = u_z, && \text{(30f)}\\
&\dot{g}_1 = -C_0 g_1 + C_2 (\nabla u)_{rr} + (C_0 C_2 + C_3)(\nabla h)_{rr}, && \text{(30g)}\\
&\dot{g}_2 = -C_0 g_2 + C_2 (\nabla u)_{\theta r} + (C_0 C_2 + C_3)(\nabla h)_{\theta r}, && \text{(30h)}
\end{aligned}
$$

and

$$
\begin{aligned}
&u_R = \bar{u}_R, \quad u_z = \bar{u}_z \quad \text{on } \partial\Omega_u,\\
&\begin{bmatrix} R\,(\sigma_{RR} + \Sigma_{RR}) & R\,(\sigma_{Rz} + \Sigma_{Rz}) \\ R\,(\sigma_{zR} + \Sigma_{zR}) & R\,(\sigma_{zz} + \Sigma_{zz}) \end{bmatrix}^T \begin{Bmatrix} n_R \\ n_z \end{Bmatrix} = \begin{Bmatrix} t_R \\ t_z \end{Bmatrix} \quad \text{on } \partial\Omega_t,
\end{aligned}
$$

where

$$
\begin{aligned}
&\sigma_{RR} = 2\mu\,(\nabla u)_{RR} + \lambda \left((\nabla u)_{RR} + (\nabla u)_{zz} + (\nabla u)_{\phi\phi} \right),\\
&\sigma_{zz} = 2\mu\,(\nabla u)_{zz} + \lambda \left((\nabla u)_{RR} + (\nabla u)_{zz} + (\nabla u)_{\phi\phi} \right),\\
&\sigma_{\phi\phi} = 2\mu\,(\nabla u)_{\phi\phi} + \lambda \left((\nabla u)_{RR} + (\nabla u)_{zz} + (\nabla u)_{\phi\phi} \right),\\
&\sigma_{Rz} = \sigma_{zR} = \mu\,((\nabla u)_{Rz} + (\nabla u)_{zR})\,,\\
&(\nabla w)_{RR} = w_{R,R}, \quad (\nabla w)_{zz} = w_{z,z}, \quad (\nabla w)_{\phi\phi} = \frac{w_R}{R},\\
&(\nabla w)_{Rz} = w_{R,z}, \quad (\nabla w)_{zR} = w_{z,R}, \qquad\qquad (w{=}u,\ v,\ h),
\end{aligned}
$$

where n_R and n_z are the R- and z-components of the outward normal vector to $\partial\Omega_t$. The coefficients C_0, ..., and C_7 are given in Eqns. (27) and (29) and components of $\mathbf{\Sigma}$ are defined in Eqn. (28); see Appendix A.2. Problem (30) inherits the boundary conditions from the original problem (18).

C Parameter choice

C.1 One-dimensional PML parameter optimization on frequency-domain

A procedure of finding an optimum set of PML parameters was studied in detail for a one-dimensional wave equation in the frequency-domain in [44]. We first summarize the procedure in [44] and introduce heuristics of choosing time-domain parameters using our example in Sec. 4.

We discretize Eqn. (5a) with $k = 0$ on $x \in [0, x_{pml}]$, in which the PML domain corresponds to $x_0 \le x$, using finite element methods of order q with

$$
s(x) = 1 + \frac{1}{\mathrm{i}} f^p(x), \tag{32}
$$

which is obtained by setting $f^e(x) = 0$ and $\frac{\omega_0}{\omega} = 1$ in Eqn. (6). We further restrict the profile of $f^p(x)$ to polynomials as:

$$f^p(x) = \beta^p \left(\frac{x - x_0}{x_{pml} - x_0} \right)^m \tag{33}$$

where m and β^p are the order and end-value of the polynomials, respectively. On solving problem (5a), one can nondimensionalize the problem to obtain a set of five independent parameters: n_{wpml}, m, β^p, n_{npw}, and q, where n_{wpml} and n_{npw} are number of wavelengths in the PML and number of nodes per wavelength, respectively. Then, for select sets of m, n_{npw}, and q, we vary β^p and n_{wpml} from 0 to 10 and plot contours of reflection coefficients. The procedure to compute the reflection coefficients are briefly explained in the following. On each element in the elastic region, $0 \leq x \leq x_0$, Eqn. (5a) produces an element-wise discrete wave operator upon finite element discretization:

$$\square := -k^2 \boldsymbol{m}_e + \boldsymbol{k}_e, \tag{34}$$

where $\boldsymbol{m}_e$ and $\boldsymbol{k}_e$ are element mass and element stiffness matrices and $k = \omega/c$ is the wave number. The wave operators (34) are then assembled to form a global stiffness matrix $\boldsymbol{K}$. Further, a set of q nodal displacements in the jth element is denoted by $\boldsymbol{u}_j$ and concatenated to form a global solution vector $\boldsymbol{U}$. The structures of $\boldsymbol{K}$ and $\boldsymbol{U}$ are schematically shown for $q = 3$ in Fig. 9. Three successive nodal displacement vectors in the elastic domain, $\boldsymbol{u}_{j-1}$, $\boldsymbol{u}_j$, and $\boldsymbol{u}_{j+1}$, satisfy a homogeneous system of discrete wave equations which characterizes wave propagation on an unbounded domain:

$$\boldsymbol{B}^T \boldsymbol{u}_{j-1} + \boldsymbol{A}\boldsymbol{u}_j + \boldsymbol{B}\boldsymbol{u}_{j+1} = \boldsymbol{0}, \tag{35}$$

as shown in Fig. 9. Substituting $\boldsymbol{u}_j = \xi^j \boldsymbol{v}$ in the homogeneous system (35), one obtains a quadratic eigenvalue problem:

$$\left[\boldsymbol{B}^T + \xi \boldsymbol{A} + \xi^2 \boldsymbol{B} \right] \boldsymbol{v} = \boldsymbol{0},$$

for which there exist two nonzero eigenvalues ξ^+ and ξ^- and corresponding eigenvectors $\boldsymbol{v}^+$ and $\boldsymbol{v}^-$, the former representing outgoing and the latter representing incoming waves so that the total solution on the homogeneous elastic media should be represented as:

$$\boldsymbol{u}_j = \left[\left(\xi^+\right)^j \boldsymbol{v}^+ \quad \left(\xi^-\right)^j \boldsymbol{v}^- \right] \begin{pmatrix} c^+ \\ c^- \end{pmatrix}. \tag{36}$$

We now compute the solution to the PML problem (5) by a standard linear solver and extract two solution vectors $\boldsymbol{u}_j$ and $\boldsymbol{u}_{j+1}$ to solve for c^+ and c^- in Eqn. (36). Specifically, we have

$$\begin{pmatrix} c^+ \\ c^- \end{pmatrix} = \begin{bmatrix} \left(\xi^+\right)^j \boldsymbol{v}^+ & \left(\xi^-\right)^j \boldsymbol{v}^- \\ \left(\xi^+\right)^{j+1} \boldsymbol{v}^+ & \left(\xi^-\right)^{j+1} \boldsymbol{v}^- \end{bmatrix}^\dagger \begin{pmatrix} \boldsymbol{u}_j \\ \boldsymbol{u}_{j+1} \end{pmatrix} \tag{37}$$

where † represents pseudo-inverse. The reflection coefficient r is given by the ratio $|c^-/c^+|$. Note that since we project the solution onto discrete modes and consider the ratio of the discrete incoming wave to the discrete outgoing wave, r represents the reflection due to discretization of the PML as well as its termination.

Figures 10a, 10b, 10c and 10d show contour plots of $\log_{10} r$ for $m = 1, 2, 3, 4$, respectively, with fixed $q = 4$ and $n_{npw} = 12$ on a grid of $(n_{wpml}, \beta^p) = [0, 10] \times [0, 10]$. With knowledge of q and n_{npw} and with an allowed level of total reflection in mind, one can readily read off an optimum set of PML parameters, n_{wpml}, β^p, and m, which can achieve the desired level of accuracy with smallest n_{wpml}.

These contour plots characterize the two kinds of reflections $r_{\text{termination}}$ and $r_{\text{discretization}}$ mentioned in Sec. 2.1. As a specific example, focus on Fig. 10c with n_{wpml} fixed at 4. Increasing β^p from zero, one observes a rapid decrease of $\log_{10} r$ up to $\beta^p \approx 1$ to achieve $\log_{10} r = -6$. If one further increase β^p, $\log_{10} r$ gradually increases. This suggests that in the first phase $r_{\text{termination}}$ given in Eqn. (4) surpasses $r_{\text{discretization}}$, while in the second phase $r_{\text{discretization}}$ surpasses $r_{\text{termination}}$. Indeed, on the region of small β^p and large n_{wpml}, a curve of a constant r, say $\bar{r}$, almost coincides with a curve produced by Eqn. (4) with $r_{\text{termination}}$ fixed at $\bar{r}$, which verifies that $r \approx r_{\text{termination}}$ in this region of parameter space. See [44] for further elaboration.

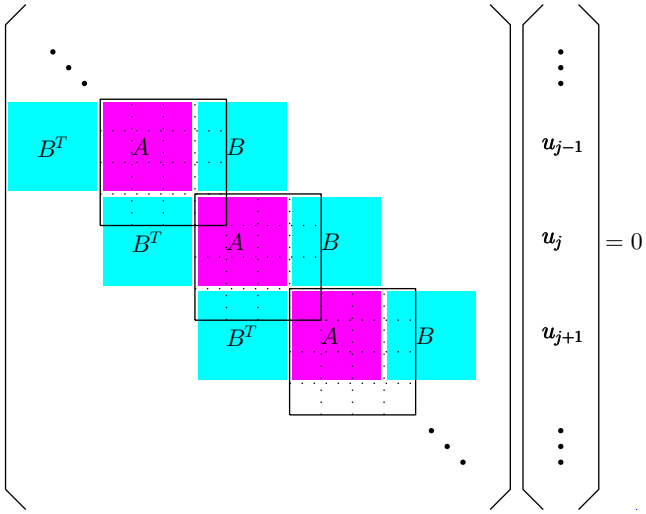

Figure 9: Schematic of one-dimensional discrete wave equation in frequency-domain on elastic medium with cubic ($q = 3$) interpolation polynomials. Each square with solid sides represents an element-wise stiffness matrix.

C.2 Parameter choice heuristics on time-domain

Heuristics for choosing PML parameters for elastodynamics in the time-domain for a given level of discretization and an order of element q are summarized below:

- Choose an characteristic frequency (ω_0 in Eqn. (6)) and wave speed c_0 and compute a characteristic wavelength λ_0.
- Compute n_{npw}, where n_{npw} denotes the number of nodes per characteristic wavelength.
- Given allowed total reflection coefficients r_{allowed}, read off an optimum pair of parameters n_{wpml} and β^p for an optimum m from contour plots for the desired q and n_{npw}, where n_{wpml} denotes the number of characteristic wavelengths in the PML.

A time-domain PML thus obtained ensures that the reflection coefficient should be r_{allowed} for a mode of frequency ω_0 since Eqn. (6) reduces to Eqn. (32) when $\omega = \omega_0$.

For our problems in Sec. 4, we choose $\omega_0 = 4\pi$ considering the pattern of the waves generated by the excitation (23). Setting $c_0 = c_s$, where c_s is the shear wave velocity, we obtain $n_{npw} \approx 12$. r_{allowed} is set to 10^{-3} as is often done in practice. We then look at Figs. 10a-10d for $m = 1, 2, 3, 4$ with fixed $n_{npw} = 12$ and $q = 4$. According to these figures, the minimum possible n_{wpml} required to achieve $r = 10^{-3}$ for $m = 1$, 2, 3, and 4 are about 1.0, 0.5, 0.6, and 0.7, respectively, so we choose to use $m = 2$. The corresponding parameters are $n_{wpml} \approx 0.5$ and $\beta^p \approx 4$. Also we make a conservative choice of $r_{pml} - r_0 = 1.5[\mu\text{m}]$ which gives $n_{wpml} \approx 0.8$. In summary, we use $\omega_0 = 4\pi$, $m = 2$, $n_{wpml} \approx 0.8$, and $\beta^p = 4$.

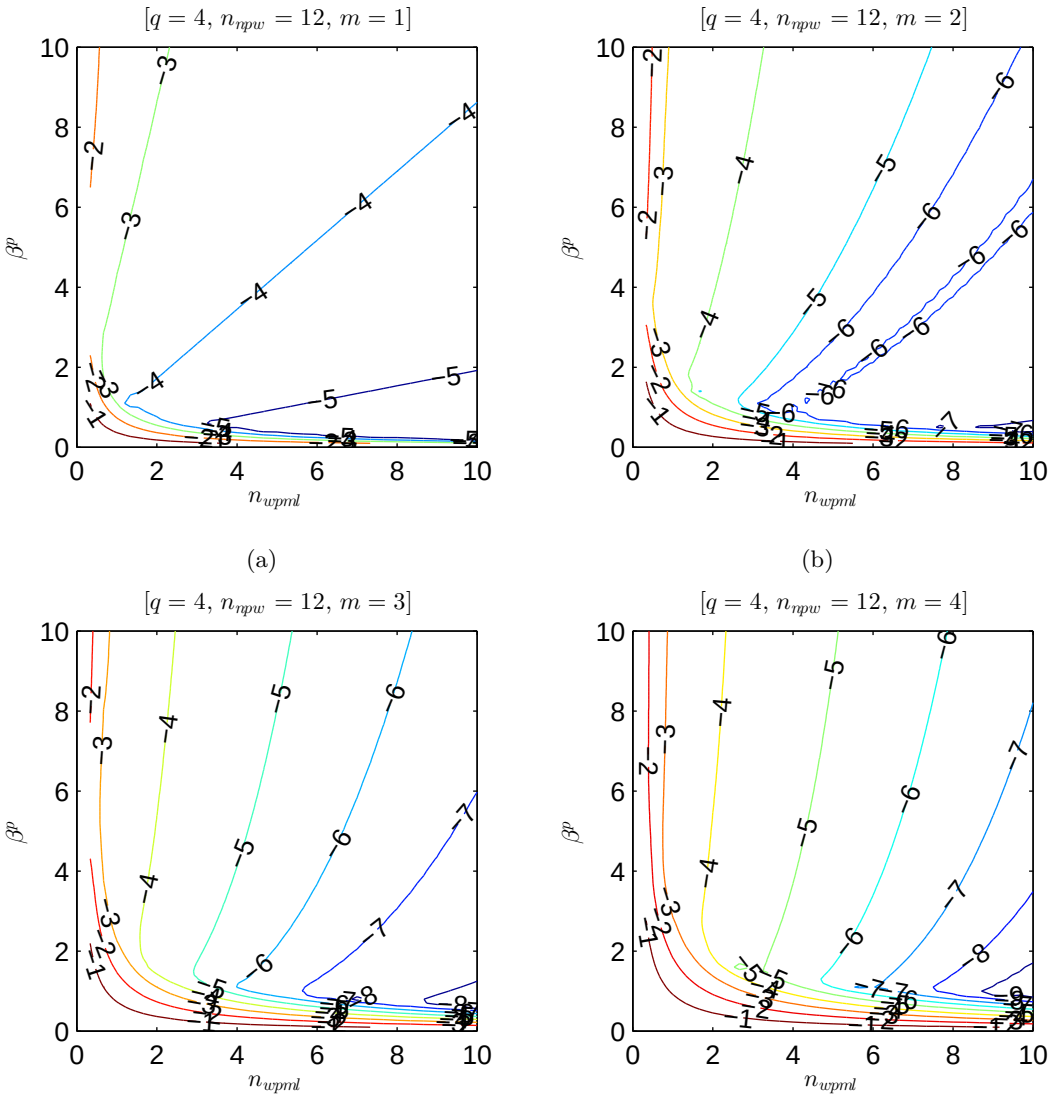

Figure 10: Contour plots of $\log_{10} r$ for (a) $m = 1$ (b) $m = 2$ (c) $m = 3$ (d) $m = 4$, fixing $q = 4$ and $n_{npw} = 12$.